Appl. Math. Mech. -Engl. Ed., **39**(12), 1691–1718 (2018)

Applied Mathematics and Mechanics (English Edition)

https://doi.org/10.1007/s10483-018-2397-9

Novel wavelet-homotopy Galerkin technique for analysis of lid-driven cavity flow and heat transfer with non-uniform boundary conditions*

Qiang YU, Hang XU†

Collaborative Innovation Center for Advanced Ship and Deep-Sea Exploration (CISSE),
State Key Laboratory of Ocean Engineering, School of Naval Architecture
Ocean and Civil Engineering, Shanghai Jiao Tong University,
Shanghai 200240, China

(Received May 15, 2018 / Revised Jul. 9, 2018)

Abstract In this paper, a brand-new wavelet-homotopy Galerkin technique is developed to solve nonlinear ordinary or partial differential equations. Before this investigation, few studies have been done for handling nonlinear problems with non-uniform boundary conditions by means of the wavelet Galerkin technique, especially in the field of fluid mechanics and heat transfer. The lid-driven cavity flow and heat transfer are illustrated as a typical example to verify the validity and correctness of this proposed technique. The cavity is subject to the upper and lower walls' motions in the same or opposite directions. The inclined angle of the square cavity is from 0 to $\pi/2$. Four different modes including uniform, linear, exponential, and sinusoidal heating are considered on the top and bottom walls, respectively, while the left and right walls are thermally isolated and stationary. A parametric analysis of heating distribution between upper and lower walls including the amplitude ratio from 0 to 1 and the phase deviation from 0 to 2π is conducted. The governing equations are non-dimensionalized in terms of the stream function-vorticity formulation and the temperature distribution function and then solved analytically subject to various boundary conditions. Comparisons with previous publications are given, showing high efficiency and great feasibility of the proposed technique.

Key words wavelet-homotopy, Galerkin technique, mixed boundary condition, lid-driven inclined cavity, non-uniform heat transfer

Chinese Library Classification O29, O357
2010 Mathematics Subject Classification 34B15, 35J60

* Citation: YU, Q. and XU, H. Novel wavelet-homotopy Galerkin technique for analysis of lid-driven cavity flow and heat transfer with non-uniform boundary conditions. *Applied Mathematics and Mechanics* (*English Edition*), **39**(12), 1691–1718 (2018) https://doi.org/10.1007/s10483-018-2397-9

† Corresponding author, E-mail: hangxu@sjtu.edu.cn

Project supported by the National Natural Science Foundation of China (Nos. 11272209, 11432009, and 11872241)

1 Introduction

In recent years, fundamental problems of mixed convection heat transfer involving natural and forced convection in lid-driven cavities have received considerable attention in science and engineering. Practical applications of such cavity flows could be found in atmospheric flow[1], lakes and reservoirs[2], nuclear reactors[3], chemical equipment[4], lubrication grooves[5], solar collectors[6], solidification process[7], and float grass production[8].

Mixed convection in a lid-driven cavity is difficult to analyze since its governing equations are coupled partial differential equations. The flow governing dimensionless parameter is the Richardson number $Ri = Gr/Re^2$, which is defined as the ratio between the Grashof number Gr and the square of the Reynolds number Re, where they represent the relative strength of the natural and forced convection flow effects[9]. The combined shear and buoyancy-driven convection is categorized into pure forced convection flow ($Ri \ll 1$), natural convection ($Ri \gg 1$), and mixed one for $Ri = 0.1 \sim 10$, of which the former two regimes are the limiting cases. Therefore, it is of great significance to understand intensively the mechanism of mixed convection.

Various configurations of mixed convection cavity flows have been investigated. For example, the upper lid-driven case was investigated in Refs. [10]–[21]. Both the top and bottom lid-driven cases were discussed in Refs. [22]–[26]. The inclination case was studied in Refs. [27]–[31]. There were also many investigations on mixed convection flow with non-uniform heated boundaries that are commonly found in the industrial process. For example, Basak et al.[32–34] carried out a series of studies on mixed convection in the lid-driven cavity with linear distribution of temperature at vertical sides or sinusoidal type[35] at the bottom. More studies were carried out by Sivasankaran et al.[36–37], Hsu and Wang[38], Al-Amiri and Khanafer[39], Abu-Nada and Chamkha[40], and Nasrin and Parvin[41].

In the above-mentioned studies, many different numerical techniques have been applied, such as the finite difference method[9], the finite volume method (FVM)[33,42], and the pseudo-spectral collocation method[43], while no wavelet technique was used. It is known that the wavelet technique has great excellence for illustration of the local details of solutions, which has been successively applied in many different fields, including signal analysis[44], fluid[45], and solid[46] mechanics. It is reasonable to suppose that this technique has better capability than other approaches to show the detailed information of vortexes and eddies. However, by now, the wavelet technique has rarely been used to solve nonlinear problems in fluid mechanics and heat transfer, owing to complex governing equations and boundary conditions. To overcome its major limitation, we introduce the homotopy idea to the Coiflets-type wavelet. This idea has been proved practicably. Several successful examples can be found in Refs. [47]–[49]. However, all of those examples were confined to handle nonlinear problems subject to homogeneous boundary conditions. None has been done on nonlinear problems with nonhomogeneous boundary conditions, which are obviously often encountered in the research of fluid mechanics and heat transfer.

In this paper, we shall extend the wavelet homotopy analysis method (wHAM) to the classical cavity flow and heat transfer problem. Similar studies have not been reported in the literature, as far as we know. The general case of the convective heat transfer in a cavity is considered. The cavity is placed on a slope with the upper and lower walls moving at constant speeds simultaneously. Both moving walls are subject to four different heating modes, including uniform, linear, exponential, and sinusoidal distributions. Comparisons with the previous results are given to testify the validity and correctness of our proposed technique. Detailed parametric investigations of nonuniform boundaries, amplitude ratio, phase deviation of temperature, and inclination of cavity are carried out for this generalized problem.

2 Mathematical description

A two-dimensional square cavity of length H is placed on a slope of inclined angle γ with its top and bottom walls moving at constant speeds U_0 and λU_0 in the same or opposite

directions and heating non-uniformly. The sketch is shown in Fig. 1, where the origin of the Cartesian coordinate system is at the bottom left corner with the x- and y-axes along the length and height of the cavity, respectively. Non-uniform temperature distributions are imposed on both horizontal walls of the enclosure. $\lambda = 0$ indicates that the bottom lid is stationary. $\lambda = 1$ and $\lambda = -1$ mean that the horizontal walls move in the same or opposite directions, respectively. It is assumed that the viscous dissipation and heat radiation are neglected. It is also assumed that the fluid properties are constant and laminar so that the conservations of mass, momentum, and energy are satisfied. The density variation is modeled according to the Boussinesq approximation, in which the variations in fluid properties other than the density are ignored, and the density ρ only appears when it is multiplied by the gravitational acceleration linearized with the temperature,

$$\rho = \rho_0(1 - \beta(T - T_0)), \tag{1}$$

where β is the thermal expansion coefficient, and ρ_0 and T_0 denote the reference state.

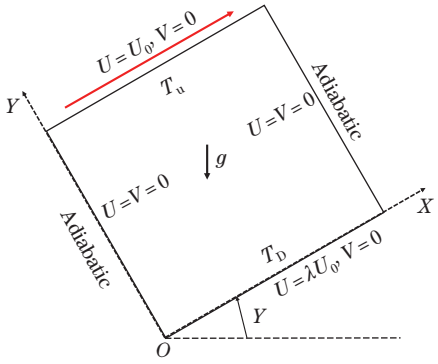

Fig. 1 Schematic diagram of inclined cavity with heat transfer

Since the flow transients are always smooth, the steady mixed convection flow in a square cavity makes sense compared with the unsteady one which plays an important role in the configurations[10]. With those assumptions, the governing equations are written as follows.

The continuity equation is

$$\frac{\partial U}{\partial X} + \frac{\partial V}{\partial Y} = 0. \tag{2}$$

The momentum equations in the X- and Y-directions are

$$U\frac{\partial U}{\partial X} + V\frac{\partial U}{\partial Y} = -\frac{1}{\rho}\frac{\partial P}{\partial X} + \nu\Big(\frac{\partial^2 U}{\partial X^2} + \frac{\partial^2 U}{\partial Y^2}\Big) - \beta(T - T_0)g\sin\gamma, \tag{3}$$

$$U\frac{\partial V}{\partial X} + V\frac{\partial V}{\partial Y} = -\frac{1}{\rho}\frac{\partial P}{\partial Y} + \nu\Big(\frac{\partial^2 V}{\partial X^2} + \frac{\partial^2 V}{\partial Y^2}\Big) - \beta(T - T_0)g\cos\gamma. \tag{4}$$

The thermal energy transport equation without internal heat production is

$$U\frac{\partial T}{\partial X} + V\frac{\partial T}{\partial Y} = \frac{k}{\rho c_p}\Big(\frac{\partial^2 T}{\partial X^2} + \frac{\partial^2 T}{\partial Y^2}\Big). \tag{5}$$

The appropriate boundary conditions are

$$\begin{cases} U=\lambda U_0, \quad V=0, \quad T=T_{\rm b}(X) \quad \text{on} \quad Y=0, \\ U=U_0, \quad V=0, \quad T=T_{\rm t}(X) \quad \text{on} \quad Y=H, \\ U=0, \quad V=0, \quad \dfrac{\partial T}{\partial Y}=0 \quad \text{on} \quad X=0, \\ U=0, \quad V=0, \quad \dfrac{\partial T}{\partial Y}=0 \quad \text{on} \quad X=H. \end{cases} \tag{6}$$

Here, U and V are the velocity components in the X- and Y-directions, respectively, P is the pressure, T is the temperature, $T_{\rm t}(X)$ and $T_{\rm b}(X)$ are the temperature distributions on the top and bottom walls, respectively, g is the acceleration of gravity, and k and c_p denote the thermal conductivity and the specific heat, respectively.

Substituting the following vorticity-stream function formulation

$$U=\frac{\partial \Psi}{\partial Y}, \quad V=-\frac{\partial \Psi}{\partial X}, \quad \Omega=\frac{\partial V}{\partial X}-\frac{\partial U}{\partial Y} \tag{7}$$

and the following dimensionless variables

$$\begin{cases} x=\dfrac{X}{H}, \quad y=\dfrac{Y}{H}, \quad u=\dfrac{U}{U_0}, \quad v=\dfrac{V}{U_0}, \\ \psi=\dfrac{\Psi}{U_0 H}, \quad \omega=\dfrac{\Omega H}{U_0}, \quad \theta=\dfrac{T-T_0}{\Delta T} \end{cases} \tag{8}$$

into the above governing equations, the dimensionless governing equations are obtained,

$$\frac{\partial \psi}{\partial y}\frac{\partial \omega}{\partial x}-\frac{\partial \psi}{\partial x}\frac{\partial \omega}{\partial y}=\frac{1}{Re}\Big(\frac{\partial^2 \omega}{\partial x^2}+\frac{\partial^2 \omega}{\partial y^2}\Big)+\frac{Gr}{Re^2}\Big(\frac{\partial \theta}{\partial x}\cos\gamma-\frac{\partial \theta}{\partial y}\sin\gamma\Big), \tag{9}$$

$$\frac{\partial \psi}{\partial y}\frac{\partial \theta}{\partial x}-\frac{\partial \psi}{\partial x}\frac{\partial \theta}{\partial y}=\frac{1}{RePr}\Big(\frac{\partial^2 \theta}{\partial x^2}+\frac{\partial^2 \theta}{\partial y^2}\Big), \tag{10}$$

where the Reynolds number Re, the Grashof number Gr, and the Prandtl number Pr are defined by

$$Re=\frac{U_0 H}{\nu}=\frac{\rho_{\rm f} U_0 H}{\mu}, \quad Gr=\frac{\beta g \Delta T H^3}{\nu^2}, \quad Pr=\frac{\nu}{\alpha}, \tag{11}$$

in which α, ν, and ΔT denote the thermal diffusivity, the dynamic viscosity, and the reference temperature difference, respectively.

Finally, we eliminate the vortices ω to obtain the final coupled dimensionless differential equations,

$$\nabla^4 \psi - RiRe\Big(\frac{\partial \theta}{\partial x}\cos\gamma-\frac{\partial \theta}{\partial y}\sin\gamma\Big)+Re\,\mathcal{N}[\psi,\psi]=0, \tag{12}$$

$$\nabla^2 \theta + PrRe\Big(\frac{\partial \psi}{\partial x}\frac{\partial \theta}{\partial y}-\frac{\partial \psi}{\partial y}\frac{\partial \theta}{\partial x}\Big)=0 \tag{13}$$

subject to the boundary conditions

$$\begin{cases} \psi=0, \quad \dfrac{\partial \psi}{\partial y}=\lambda, \quad \theta=\theta_{\rm b}(x) \quad \text{on} \quad y=0, \\ \psi=0, \quad \dfrac{\partial \psi}{\partial y}=1, \quad \theta=\theta_{\rm t}(x) \quad \text{on} \quad y=1, \\ \psi=0, \quad \dfrac{\partial \psi}{\partial x}=0, \quad \dfrac{\partial \theta}{\partial x}=0 \quad \text{on} \quad x=0, \\ \psi=0, \quad \dfrac{\partial \psi}{\partial x}=0, \quad \dfrac{\partial \theta}{\partial x}=0 \quad \text{on} \quad x=1, \end{cases} \tag{14}$$

where $Ri = Gr/Re^2$ is the Richardson number, ∇^2 is the Laplace operator, ∇^4 is the Biharmonic operator, elaborated in the Cartesian coordination system by

$$\nabla^4 = \nabla^2\nabla^2 = \frac{\partial^4}{\partial x^4} + 2\frac{\partial^4}{\partial x^2\partial y^2} + \frac{\partial^4}{\partial y^4},$$

and the nonlinear operator $\mathcal{N}$ for arbitrary functions F and G is

$$\mathcal{N}[F,G] = \frac{\partial F}{\partial x}\frac{\partial^3 G}{\partial x^2\partial y} + \frac{\partial F}{\partial x}\frac{\partial^3 G}{\partial y^3} - \frac{\partial F}{\partial y}\frac{\partial^3 G}{\partial x^3} - \frac{\partial F}{\partial y}\frac{\partial^3 G}{\partial x\partial y^2}.$$

It is known that the no-slip boundary conditions (14) have been widely used to describe one side or two-side lid-driven cavities. However, there are non-physical singularities at four corners, which have to be considered in the computation.

The local Nusselt number $Nu = -\nabla\theta\cdot\boldsymbol{n} = -\frac{\partial\theta}{\partial n}$ is a key factor to measure the heat transfer rate, which can be defined as

$$Nu_{\mathrm{b}} = \left.\frac{\partial\theta}{\partial y}\right|_{y=0}, \quad Nu_{\mathrm{t}} = -\left.\frac{\partial\theta}{\partial y}\right|_{y=1}, \tag{15}$$

where Nu_{b} and Nu_{t} are the Nusselt numbers on the bottom and top walls, respectively.

The average Nusselt numbers along the horizontal surfaces demonstrating the level of heat transfer rate are defined by

$$\overline{Nu}_{\mathrm{b}} = \int_0^1 Nu_{\mathrm{b}}\mathrm{d}x, \quad \overline{Nu}_{\mathrm{t}} = \int_0^1 Nu_{\mathrm{t}}\mathrm{d}x. \tag{16}$$

3 Wavelet-homotopy technique

In the generalized orthogonal Coiflet system, when an arbitrary function $f(x)$ is approximated by the Coiflets, the approaching precision only depends on its resolution level and wavelet properties irrelevant to $f(x)$. Hence, the generalized orthogonal Coiflet basis can be employed as the expression functions for approximating solutions of nonlinear problems to be solved. In doing so, the governing equations (12) and (13) are first transformed into a group of linear ones by the homotopy analysis method (HAM) technique. The highly accurate generalized orthogonal Coiflet series solutions are given by the wavelet Galerkin method.

3.1 Linearization

The linearization of the nonlinear systems (12) and (13) is fulfilled by means of the HAM via constructing the zero deformation equations,

$$(1-p)\mathcal{L}_\psi[\Phi(x,y;p) - \Phi(x,y;0)] = p\,c_1\mathcal{N}_\psi[\Phi(x,y;p),\Theta(x,y;p)], \tag{17a}$$

$$(1-p)\mathcal{L}_\theta[\Theta(x,y;p) - \Theta(x,y;0)] = p\,c_2\mathcal{N}_\theta[\Phi(x,y;p),\Theta(x,y;p)], \tag{17b}$$

where $p\in[0,1]$ is an embedding parameter, $\mathcal{L}_\psi$ and $\mathcal{L}_\theta$ are the linear operators, c_1 and c_2 are the convergence-control parameters, $\Phi(x,y;p)$ and $\Theta(x,y;p)$ are the mappings of $\psi(x,y)$ and $\theta(x,y)$, and $\mathcal{N}_\psi[\Phi,\Theta]$ and $\mathcal{N}_\theta[\Phi,\Theta]$ are the nonlinear operators defined by

$$\mathcal{N}_\psi[\Phi,\Theta] = \nabla^4\Psi - RiRe\Big(\frac{\partial\Theta}{\partial x}\cos\gamma - \frac{\partial\Theta}{\partial y}\sin\gamma\Big) + Re\,\mathcal{N}[\Psi,\Psi], \tag{18a}$$

$$\mathcal{N}_\theta[\Phi,\Theta] = \nabla^2\Theta + PrRe\Big(\frac{\partial\Psi}{\partial x}\frac{\partial\Theta}{\partial y} - \frac{\partial\Psi}{\partial y}\frac{\partial\Theta}{\partial x}\Big). \tag{18b}$$

For $p=0$ and $p=1$, we have

$$\begin{cases} \Psi(x,y;0)=\psi_0(x,y), & \Psi(x,y;1)=\psi(x,y), \\ \Theta(x,y;0)=\theta_0(x,y), & \Theta(x,y;1)=\theta(x,y). \end{cases} \tag{19}$$

It should be pointed that as p varies from 0 to 1, the initial guesses ψ_0 and θ_0 are transformed to the desired solutions ψ and θ. Therefore, the Taylor expansions for Ψ and Θ with respect to p are illustrated as

$$\Psi(x,y;p)=\psi_0(x,y)+\sum_{M=1}^{+\infty}\psi_M(x,y)p^M, \tag{20}$$

$$\Theta(x,y;p)=\theta_0(x,y)+\sum_{M=1}^{+\infty}\theta_M(x,y)p^M, \tag{21}$$

where

$$\begin{cases} \psi_M(x,y)=\dfrac{1}{M!}\dfrac{\partial^M\Psi(x,y;p)}{\partial p^M}\Big|_{p=0}, \\ \theta_M(x,y)=\dfrac{1}{M!}\dfrac{\partial^M\Theta(x,y;p)}{\partial p^M}\Big|_{p=0}. \end{cases} \tag{22}$$

The auxiliary linear operators, the initial guesses, and the convergence control parameters are appropriately selected so that the Taylor series converge at $p=1$. The homotopy series solutions are determined as

$$\psi(x,y)=\psi_0(x,y)+\sum_{M=1}^{+\infty}\psi_M(x,y)p^M, \tag{23}$$

$$\theta(x,y)=\theta_0(x,y)+\sum_{M=1}^{+\infty}\theta_M(x,y)p^M. \tag{24}$$

Differentiating Eqs. (17a) and (17b) M times with respect to p, then dividing them by $M!$, and finally setting $p=0$, we obtain the Mth-order deformation equations,

$$\mathcal{L}_\psi(\psi_M-\kappa_M\psi_{M-1})=c_1(\nabla^4\psi_{M-1}+S^\theta_{M-1}+R^\psi_M), \tag{25}$$

$$\mathcal{L}_\theta(\theta_M-\kappa_M\theta_{M-1})=c_2(\nabla^2\theta_{M-1}+R^\theta_M), \tag{26}$$

where

$$S^\theta_{M-1}=-RiRe\Big(\frac{\partial\theta_{M-1}}{\partial x}\cos\gamma-\frac{\partial\theta_{M-1}}{\partial y}\sin\gamma\Big),$$

$$R^\psi_M=Re\sum_{s=0}^{M-1}\mathcal{N}(\psi_s,\psi_{M-1-s}),$$

$$R^\theta_M=PrRe\sum_{s=0}^{M-1}\Big(\frac{\partial\psi_s}{\partial x}\frac{\partial\theta_{M-1-s}}{\partial y}-\frac{\partial\psi_s}{\partial y}\frac{\partial\theta_{M-1-s}}{\partial x}\Big)$$

with

$$\kappa_M=\begin{cases} 0, & M\leqslant 1, \\ 1, & M>1. \end{cases} \tag{27}$$

3.2 Generalized orthogonal Coiflets selection

Following Liu et al.[50] and Zhou and Wang[51], an arbitrary function $\widetilde{f}(x)$ is approximated by Coiflets,

$$\widetilde{f}(x) \approx \sum_{k=2-3N+M_1}^{2^j-1+M_1} \widetilde{f}\Big(\frac{k}{2^j}\Big)\phi(2^j x - k + M_1), \tag{28}$$

where N is the vanishing moment, M_1 is the first-order vanishing moment, and ϕ is the wavelet basis. Note that the coefficients of Coiflets series are the approximate values of the function middle points. In order to include nonhomogeneous boundary information into the Coiflets, inspired by Liu et al.[50] and Zhou and Wang[51], we construct the boundary Coiflets by adding the spline functions to make up for the missing derivative information on boundaries, which can be written as

$$\hat{f}(x) = \begin{cases} \displaystyle\sum_{k=0}^{3}\Big(f_{j,k}T_{0,k}(x) + \frac{\alpha_{0,k}}{k!}x^k\Big), & x \in (-\delta, 0), \\ f(x), & x \in [0,1], \\ \displaystyle\sum_{k=0}^{3}\Big(f_{j,2^j-k}T_{1,k}(x) + \frac{\alpha_{1,k}}{k!}(x-1)^k\Big), & x \in (1, 1+\delta), \end{cases} \tag{29}$$

where $T_{0,k}(x)$ and $T_{1,k}(x)$ are the modification functions

$$T_{0,k}(x) = \sum_{i=0}^{3}\Big(\frac{p_{i,k}^0}{i!}\Big)x^i, \quad T_{1,k}(x) = \sum_{i=0}^{3}\Big(\frac{p_{i,k}^1}{i!}\Big)(x-1)^i, \tag{30}$$

in which $p_{i,k}^0$ and $p_{i,k}^1$ are coefficients, determined by the following coefficient matrices $\boldsymbol{P}_0^c$ and $\boldsymbol{P}_1^c$:

$$\boldsymbol{P}_0^c = \begin{pmatrix} 1 & 0 & 0 & 0 \\ -11/6 & 3 & -3/2 & 1/3 \\ 2 & -5 & 4 & -1 \\ -1 & 3 & -3 & 1 \end{pmatrix}, \quad \boldsymbol{P}_1^c = \begin{pmatrix} 1 & 0 & 0 & 0 \\ 11/6 & -3 & 3/2 & -1/3 \\ 2 & -5 & 4 & -1 \\ 1 & -3 & 3 & -1 \end{pmatrix}.$$

On substitution of Eq. (29) into Eq. (28), we finally obtain

$$f(x) = \begin{cases} \displaystyle\sum_{k=0}^{3} f_{j,k}\Big(\sum_{i=2-3N+M_1}^{-1} T_{0,k}\Big(\frac{i}{2^j}\Big)\phi_{j,i} + \phi_{j,k}\Big) \\ \displaystyle + \sum_{k=0}^{3}\frac{\alpha_{0,k}}{k!}\Big(\sum_{i=2-3N+M_1}^{-1}\Big(\frac{i}{2^j}\Big)^k\phi_{j,i}\Big), \quad k \in [0,3], \\ \displaystyle\sum_{k=4}^{2^j-4} f_{j,k}\phi_{j,k}, \quad k \in [4, 2^j-4], \\ \displaystyle\sum_{k=2^j-3}^{2^j} f_{j,k}\Big(\sum_{i=2^j+1}^{2^j-1+M_1} T_{1,2^j-k}\Big(\frac{i}{2^j}\Big)\phi_{j,i} + \phi_{j,k}\Big) \\ \displaystyle + \sum_{k=0}^{3}\frac{\alpha_{1,k}}{k!}\Big(\sum_{i=2^j+1}^{2^j-1+M_1}\Big(\frac{i}{2^j}-1\Big)^k\phi_{j,i}\Big), \quad k \in [2^j-3, 2^j], \end{cases} \tag{31}$$

where

$$\phi_{j,i} = \phi(2^j x - i + M_1), \quad \phi_{j,k} = \phi(2^j x - k + M_1).$$

Taking Eq. (31) into account, the targeted approximation of $f(x)$ is divided into two parts. One is the generalized Coiflets with the polynomial interpolation modifications, written by

$$\varphi_{j,k}(x)=\begin{cases}\displaystyle\sum_{i=2-3N+M_1}^{-1}T_{0,k}\Big(\frac{i}{2^j}\Big)\phi_{j,i}+\phi_{j,k}, & k\in[0,3],\\ \displaystyle\sum_{k=4}^{2^j-4}\phi_{j,k}, & k\in[4,2^j-4],\\ \displaystyle\sum_{i=2^j+1}^{2^j-1+M_1}T_{1,2^j-k}\Big(\frac{i}{2^j}\Big)\phi_{j,i}+\phi_{j,k}, & k\in[2^j-3,2^j].\end{cases}\tag{32}$$

The other is the boundary wavelets expressed by

$$\begin{cases}\varpi_{j,a}^0(x)=\displaystyle\sum_{i=2-3N+M_1}^{-1}\frac{1}{a!}\Big(\frac{i}{2^j}\Big)^a\phi_{j,i},\\ \varpi_{j,a}^1(x)=\displaystyle\sum_{i=2^j+1}^{2^j-1+M_1}\frac{1}{a!}\Big(\frac{i}{2^j}-1\Big)^a\phi_{j,i},\end{cases}\tag{33}$$

where the superscripts 0 and 1 correspond to the left and right boundaries, respectively, and the subscript a relates to orders.

3.3 Coiflets selection and approaching process

Taking the inhomogeneous boundary conditions (14) into consideration, we need to construct the appropriate Coiflets to approximate ψ and θ. The procedure is listed below.

Firstly, we determine the quantities of needful types of Coiflets by defining the following boundary matrices:

$$h_{j,k}^{\psi,x}(x)=\varphi_{j,k}(x)|_{p_{0,1,i}\to0,p_{1,1,i}\to0},\quad h_{j,l}^{\psi,y}(y)=\varphi_{j,l}(y)|_{p_{0,1,i}\to0,p_{1,1,i}\to0},\tag{34}$$

$$h_{j,k}^{\theta,x}(x)=\varphi_{j,k}(x)|_{p_{0,1,i}\to0,p_{1,1,i}\to0},\quad h_{j,l}^{\theta,y}(y)=\varphi_{j,l}(y).\tag{35}$$

Thus, the boundary Coiflets related to the different orders of derivative are subject to the nonhomogeneous Neumann boundaries,

$$\varpi_{j,\mathrm{b}}(x)=\varpi_{j,1}^0(x),\quad \varpi_{j,\mathrm{t}}(x)=\varpi_{j,1}^1(x).\tag{36}$$

As a result, the dimensionless stream function and the temperature for Mth-order solutions are expressed by Coiflets as

$$\psi_M(x,y)\approx\sum_{k'=1}^{2^j-1}\sum_{l'=1}^{2^j-1}\psi_M\Big(\frac{k'}{2^j},\frac{l'}{2^j}\Big)h_{j,k'}^{\psi,x}(x)h_{j,l'}^{\psi,y}(y)+(1-\chi_{M+1})B_\psi(x,y),\tag{37}$$

$$\theta_M(x,y)\approx\sum_{k=0}^{2^j}\sum_{l'=1}^{2^j-1}\theta_M\Big(\frac{k}{2^j},\frac{l'}{2^j}\Big)h_{j,k}^{\theta,x}(x)\varphi_{j,l'}^{\theta,y}(y)+(1-\chi_{M+1})B_\theta(x,y),\tag{38}$$

where the boundary parts $B_\psi(x,y)$ and $B_\theta(x,y)$ correspond to the Dirichlet and Neumann types,

$$\begin{cases}B_\psi(x,y)=\displaystyle\sum_{k=0}^{2^j}h_{j,k}^{\psi,x}(x)(\lambda\,\varpi_{j,\mathrm{b}}(y)+\varpi_{j,\mathrm{t}}(y)),\\ B_\theta(x,y)=\displaystyle\sum_{k=0}^{2^j}h_{j,k}^{\theta,x}(x)\Big(\theta_\mathrm{b}\Big(\frac{k}{2^j}\Big)\varphi_{j,0}^{\theta,y}(y)+\theta_\mathrm{t}\Big(\frac{k}{2^j}\Big)\varphi_{j,2^j}^{\theta,y}(y)\Big).\end{cases}\tag{39}$$

According to the general Gaussian integration method[51], the linear and nonlinear operators $\mathcal{L}$ and $\mathcal{N}$ acting on the approximating functions are converted to

$$\mathcal{R}[\widetilde{f}(x)] \approx \mathcal{R}[P^j \widetilde{f}(x)] = \sum_{k=2-3N+M_1}^{2^j-1+M_1} \widetilde{f}\Big(\frac{k}{2^j}\Big)\mathcal{R}[\varphi_{j,k}(x)], \quad \mathcal{R} = \mathcal{L}, \mathcal{N}. \tag{40}$$

Therefore, based on the above criterion, the fields of vorticity and velocity in the x- and y-directions are reconstituted by

$$\omega(x,y) = -\sum_{k'=1}^{2^j-1}\sum_{l'=1}^{2^j-1} \psi\Big(\frac{k'}{2^j}, \frac{l'}{2^j}\Big)(h^{(2)}_{j,k'}(x)h_{j,l'}(y) + h_{j,k'}(x)h^{(2)}_{j,l'}(y)) + B_\omega, \tag{41}$$

$$u(x,y) = \sum_{k'=1}^{2^j-1}\sum_{l'=1}^{2^j-1} \psi\Big(\frac{k'}{2^j}, \frac{l'}{2^j}\Big)h_{j,k'}(x)h^{(1)}_{j,l'}(y) + B_u, \tag{42}$$

$$v(x,y) = -\sum_{k'=1}^{2^j-1}\sum_{l'=1}^{2^j-1} \psi\Big(\frac{k'}{2^j}, \frac{l'}{2^j}\Big)h^{(1)}_{j,k'}(x)h_{j,l'}(y) + B_v, \tag{43}$$

where the boundary parts are

$$B_\omega = -\sum_{k=0}^{2^j} h^{(2)}_{j,k}(x)(\lambda\,\varpi_{j,\mathrm{b}}(y) + \omega_{j,\mathrm{t}}(y)) + h_{j,k}(x)(\lambda\,\varpi^{(2)}_{j,\mathrm{b}}(y) + \varpi^{(2)}_{j,\mathrm{t}}(y)),$$

$$B_u = \sum_{k=0}^{2^j} h_{j,k}(x)(\lambda\,\varpi^{(1)}_{j,\mathrm{b}}(y) + \varpi^{(1)}_{j,\mathrm{t}}(y)),$$

$$B_v = -\sum_{k=0}^{2^j} h^{(1)}_{j,k}(x)(\lambda\,\varpi_{j,\mathrm{b}}(y) + \varpi_{j,\mathrm{t}}(y)).$$

Finally, we substitute Eq. (38) into Eqs. (15) and (16) to define Coiflets constitution of local and average Nusselt numbers,

$$\begin{cases} Nu_{\mathrm{b}}(x) = \displaystyle\sum_{k=0}^{2^j} h_{j,k}(x) \sum_{l'=1}^{2^j-1} \theta\Big(\frac{k}{2^j}, \frac{l'}{2^j}\Big)\varphi^{(1)}_{j,l'}(0) + B^{\mathrm{b}}_{Nu}, \\ Nu_{\mathrm{t}}(x) = -\displaystyle\sum_{k=0}^{2^j} h_{j,k}(x) \sum_{l'=1}^{2^j-1} \theta\Big(\frac{k}{2^j}, \frac{l'}{2^j}\Big)\varphi^{(1)}_{j,l'}(1) + B^{\mathrm{t}}_{Nu}, \end{cases} \tag{44}$$

$$\begin{cases} \overline{Nu}_{\mathrm{b}} = \displaystyle\sum_{k=0}^{2^j} \widetilde{h}_{j,k} \sum_{l'=1}^{2^j-1} \theta\Big(\frac{k}{2^j}, \frac{l'}{2^j}\Big)\varphi^{(1)}_{j,l'}(0) + B^{\mathrm{b}}_{\overline{Nu}}, \\ \overline{Nu}_{\mathrm{t}} = -\displaystyle\sum_{k=0}^{2^j} \widetilde{h}_{j,k} \sum_{l'=1}^{2^j-1} \theta\Big(\frac{k}{2^j}, \frac{l'}{2^j}\Big)\varphi^{(1)}_{j,l'}(1) + B^{\mathrm{t}}_{\overline{Nu}}, \end{cases} \tag{45}$$

where

$$B_{Nu}^{\mathrm{b}}=\sum_{k=0}^{2^j}h_{j,k}(x)\Big(\theta_{\mathrm{b}}\Big(\frac{k}{2^j}\Big)\varphi_{j,0}^{(1)}(0)+\theta_{\mathrm{t}}\Big(\frac{k}{2^j}\Big)\varphi_{j,2^j}^{(1)}(0)\Big),$$

$$B_{Nu}^{\mathrm{t}}=-\sum_{k=0}^{2^j}h_{j,k}(x)\Big(\theta_{\mathrm{b}}\Big(\frac{k}{2^j}\Big)\varphi_{j,0}^{(1)}(1)+\theta_{\mathrm{t}}\Big(\frac{k}{2^j}\Big)\varphi_{j,2^j}^{(1)}(1)\Big),$$

$$B_{\widetilde{N}u}^{\mathrm{b}}=\sum_{k=0}^{2^j}\widetilde{h}_{j,k}\Big(\theta_{\mathrm{b}}\Big(\frac{k}{2^j}\Big)\varphi_{j,0}^{(1)}(0)+\theta_{\mathrm{t}}\Big(\frac{k}{2^j}\Big)\varphi_{j,2^j}^{(1)}(0)\Big),$$

$$B_{\widetilde{N}u}^{\mathrm{t}}=-\sum_{k=0}^{2^j}\widetilde{h}_{j,k}\Big(\theta_{\mathrm{b}}\Big(\frac{k}{2^j}\Big)\varphi_{j,0}^{(1)}(1)+\theta_{\mathrm{t}}\Big(\frac{k}{2^j}\Big)\varphi_{j,2^j}^{(1)}(1)\Big),$$

$$\widetilde{h}_{j,k}=\int_0^1 h_{j,k}(x)\mathrm{d}x.$$

Finally, linear operators are selected as $\mathcal{L}_\psi=\nabla^4$ and $\mathcal{L}_\theta=\nabla^2$. We construct the iterating equations by substituting Eqs. (37) and (38) into the high order HAM deformation equations (25) and (26), with the consideration of criterion Eq. (40). Detailed precesses are illustrated in Appendix B along with some definitions in Ref. [49].

In order to accelerate the solution convergence, the iteration HAM (iHAM) technique[52] is introduced. In doing so, we continuously replace the initial guesses by Mth-order approximations to adjust the trajectory of solutions from the initial guesses to the exact ones. The iteration formula is

$$F_{\mathrm{iter}}=F_{\mathrm{initial}}+\sum_{i=1}^{M}F_i(x,y)\to F_{\mathrm{initial}},\quad F=\psi,\theta. \tag{46}$$

To evaluate the validity of our solutions, an error function E_{Res} is defined as an indicator for checking convergence of Mth-order solutions. It works well for nonlinear problems without analytical solutions and is written by

$$E_{\mathrm{Res}}(F_M)=||F_M(x)||_{L^2(\boldsymbol{R})}\approx\frac{1}{(2^j+1)^2}\sum_{k=0}^{2^j}\sum_{l=0}^{2^j}F_M\Big(\frac{k}{2^j},\frac{l}{2^j}\Big)^2,\quad F=\psi,\theta. \tag{47}$$

If analytical solutions exist, we define the error distribution function as

$$E(x,y)=|F(x,y)-F_{\mathrm{e}}(x,y)|^2, \tag{48}$$

where $F(x,y)$ denotes analytical solutions, and $F_{\mathrm{e}}(x,y)$ denotes computational results. It can help us know exactly the error distribution at a certain point. The absolute error between the analytical solutions and our approximations is calculated by using the following error function:

$$E_{\mathrm{SQ}}(F)=||E||_{L^2(\boldsymbol{R})}\approx\frac{1}{(2^j+1)^2}\sum_{k=0}^{2^j}\sum_{l=0}^{2^j}\Big(F\Big(\frac{k}{2^j},\frac{l}{2^j}\Big)-F_{\mathrm{e}}\Big(\frac{k}{2^j},\frac{l}{2^j}\Big)\Big)^2, \tag{49}$$

where $F=\psi,\theta$ are the Coiflets approximations, and $F_{\mathrm{e}}=\psi_{\mathrm{e}},\theta_{\mathrm{e}}$ are the analytical ones.

4 Validation

At the beginning of our analysis, we validate the efficiency of our proposed technique by three steps. First, we compare our Coiflets solutions with the exact ones that exist in very particular cases. Then, a comparison of our solutions for the pure cavity flow with the previous published results is made for check of the accuracy. Finally, a further comparison of our solutions with other numerical ones available in the literature for general cases of mixed convection in the cavity ($Gr = 10^3 \sim 10^6, Re = 1 \sim 10^3$) is given for testification of the generalization of our proposed technique.

We first check the convergence of our solutions by comparing them with the exact ones. Note that, for $Re = 100, Gr = 100$, and $\lambda = 0$, append the following additional items P and Q defined in Appendix A on the right-hand side of Eqs. (12) and (13).

As shown in Fig. 2, the absolute error E_{SQ} between our solutions and the exact ones reduces very quickly as the iteration increases. We also notice that the convergence rate can be improved as the resolution level j enlarges. Further to check the accuracy of our solutions, we list the relative and absolute errors of $\psi(x, y)$ and $\theta(x, y)$ in Table 1. It is found that all errors reduce rapidly as the resolution level j increases from 3 to 5. It is also noticed from the table that the error for $j = 6$ is not obviously superior to that for $j = 5$, but the computational time is much longer. In order to balance precision and efficiency, the resolution level $j = 5$ is selected in the following computations so that the Coiflets series solutions contain 31×31 and 31×33 items for the stream and temperature approximations, respectively.

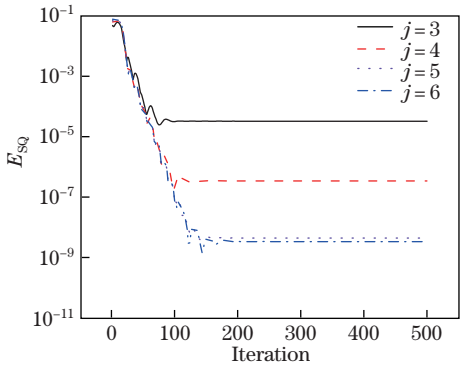

Fig. 2 E_{SQ} of temperature compared with exact solutions at different resolution levels $j = 3, 4, 5, 6$ when $Re = 100$ and $Gr = 100$ (color online)

Table 1 Precision verification of E_{Res} and E_{SQ} for stream function ψ and temperature θ at different resolution levels ($M = 5$ and iteration is 100)

Level	$E_{\mathrm{Res}}(\psi)$	$E_{\mathrm{SQ}}(\psi)$	$E_{\mathrm{Res}}(\theta)$	$E_{\mathrm{SQ}}(\theta)$	CPU time/s
$j = 3$	4.85×10^{-16}	6.89×10^{-7}	4.69×10^{-15}	2.63×10^{-5}	8.28
$j = 4$	5.15×10^{-16}	9.66×10^{-9}	1.52×10^{-16}	2.78×10^{-7}	92.06
$j = 5$	3.31×10^{-16}	1.21×10^{-10}	1.25×10^{-16}	3.56×10^{-9}	659.25
$j = 6$	2.02×10^{-13}	3.83×10^{-10}	1.29×10^{-12}	2.73×10^{-9}	3 966.52

Further to assess the accuracy of our solutions, we compare them with the previously published results for the pure lid driven cavity flow[53–56]. It is known from Eq. (12) that for the case of $Gr = 0$, the problem is reduced to the classical cavity flow. Many numerical computations are available for various configurations of cavity flow with upper lid driven. We compare our results with theirs, as illustrated hereinafter. The comparisons of our results for the values

of the minimum stream function ψ, the minimum and maximum velocity components of the flow field at midsections $x, y = 0.5$, and their locations with those given by Rubin et al.[57], Schreiber and Keller[58], Vanka[59], Hou et al.[60], Goyon[61], Barragy and Carey[62], Zhang[63], Gupta and Kalita[64], Erturk et al.[65], and Marchi et al.[56] are shown in Tables 2 and 3. Excellent agreement is found. Furthermore, by comparing our results with those given by Ghia et al.[53], Botella and Peyret[54], Bruneau and Saad[55], and Marchi et al.[56] for distributions of velocity at sections $x, y = 1/2$, it is found that our results agree well with theirs, showing good precision of our proposed technique, as illustrated in Fig. 3.

Table 2 Minimum $\psi_{\min}$ and its location of cavity flow without heat transfer $Gr = 0$ when $Re = 1\,000$ at resolution level $j = 6$ by first-order iHAM ($M = 1$) with iteration of 6 000

Result	$-\psi_{\min}$	$x(\psi_{\min})$	$y(\psi_{\min})$
Rubin and Khosla[57]	0.114 000 000	–	–
Ghia et al.[53]	0.117 929 000	0.531 30	0.562 50
Schreiber and Keller[58]	0.118 940 000	0.528 57	0.564 29
Vanka[59]	0.117 300 000	0.543 80	0.562 50
Hou et al.[60]	0.117 800 000	0.533 30	0.564 70
Goyon[61]	0.115 700 000	–	–
Barragy and Carey[62]	0.118 930 000	–	–
Botella and Peyret[54]	0.118 936 600	0.530 80	0.565 20
Zhang[63]	0.118 806 000	0.531 25	0.562 50
Gupta and Kalita[64]	0.117 000 000	0.525 00	0.562 50
Erturk et al.[65]	0.118 942 000	0.530 00	0.565 00
Bruneau and Saad[55]	0.118 920 000	0.531 25	0.565 43
Marchi et al.[56]	0.118 936 708	0.531 25	0.565 43
Present work ($j = 6$)	0.118 950 978	0.531 25	0.562 50

Table 3 Results of minimum velocity $u_{\min}$ at $x = 0.5$, minimum and maximum velocities $u_{\min}, u_{\max}$ at $y = 0.5$, and their locations by the present approach with $c_1 = -5/1\,000$, iteration of 6 000, and $M = 1$ compared with Ref. [56] for classical problem when $Re = 1\,000$ and $j = 6$

Variable	This work ($j = 6$)	Ref. [56]
$u_{\min}$	$-3.884\,333\,59\times10^{1}$	$-3.885\,721\times10^{1}$
$v_{\max}$	$3.777\,338\,1\times10^{1}$	$3.769\,471\times10^{1}$
$v_{\min}$	$-5.288\,102\,67\times10^{1}$	$-5.270\,56\times10^{1}$
$y(u_{\min})$	0.171 875	0.171 39
$x(v_{\max})$	0.161 875	0.157 71
$x(v_{\min})$	0.906 250	0.909 67
CPU time/s	9 038.5	216 000

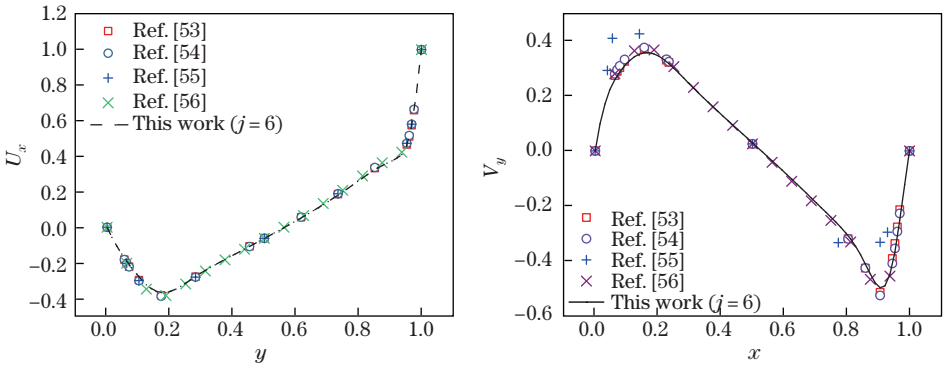

(a) Horizontal velocity U_x at $x = 0.5$ (b) Vertical velocity V_y at $y = 0.5$

Fig. 3 Horizontal and vertical velocities U_x, V_y through centerlines $x = 0.5$ and $y = 0.5$ of cavity flow at $Re = 1\,000$ compared with results by Ghia et al.[53], Botella and Peyret[54], Bruneau and Saad[55], and Marchi et al.[56] (color online)

The average Nusselt numbers, which are physically important quantities to measure the ratio of the conductive thermal resistance to the convective thermal resistance of the fluid, are also calculated via the reconstitution algorithm denoted in Eq. (45) when $Gr = 100$ and $Re = 1 \sim 1\,000$, as shown in Table 4. It is clearly shown from the table that our solutions match all of those previous results given by Iwatsu et al.[9], Khanafer and Chamkha[11], Waheed[67], Tiwari and Das[16], Ismael et al.[24], Sheremet and Pop[25], Ahmed[68], Sharif[27], Sivasankaran et al.[30], and Abu-Nada and Chamkha[40]. Besides, the local Nusselt number $Nu_{\rm b}$ and the velocity at midsections $x, y = 0.5$ by our approach are also in excellent agreement with those by the FVM using SIMPLEC algorithms[69], as shown in Fig. 4.

Table 4 Comparison of average Nusselt number computed in this work with those of other authors when $Gr = 100$

Result	Re				
	1	100	400	500	1 000
Iwatsu et al.[9]	–	1.940 000 000	3.840 000 000	–	6.330 000
Khanafer and Chamkha[11]	–	2.020 000 000	4.040 000 000	–	6.420 000
Waheed[67]	1.000 330	2.031 160 000	4.024 620 000	4.526 710 000	6.484 230
Tiwari and Das[16]	–	2.100 000 000	3.850 000 000	–	6.330 000
Ismael et al.[24]	1.019 700	2.080 000 000	4.036 000 000	4.548 000 000	6.259 900
Sheremet and Pop[25]	1.000 330	2.049 375 000	4.098 260 000	4.617 900 000	6.703 450
Ahmed[68]	1.000 899	2.105 628 000	4.221 871 000	4.599 386 000	6.494 660
Sharif[27]	–	–	4.050 000 000	–	6.550 000
Sivasankaran et al.[30]	–	–	4.090 000 000	–	6.480 000
Abu-Nada and Chamkha[40]	1.010 134	2.090 837 000	4.162 057 000	4.663 689 000	6.551 615
Present work ($j = 5$)	1.001 500	2.016 011 645	4.358 077 160	5.104 841 965	–
Present work ($j = 6$)	1.000 042	2.031 620 534	4.076 247 807	4.579 048 000	6.415 240

In the following, we make comparisons for $Gr \neq 0$. In this more general case, following the previous studies[9], it is assumed that the top wall uniformly moves and heats, while the bottom wall keeps fixed, and both the left and right walls are adiabatic and stationary. Note that in this configuration, the jump discontinuity of the velocity and temperature at the corner points exists, which corresponds to computational singularities contributing to the boundaries of the Dirichlet and Neumann types for θ and ψ. Different from the previous numerical results with special treatment by assuming the average temperature of two walls at the corner to keep the adjacent grid-nodes at respective wall temperatures[66], or obtaining optimal grid size invariant to grid by the intersection of the two differentially heated boundaries[33], we do not need any particular treatment for boundary conditions. The only thing we need to do is to adjust the vanishing moment and resolution level of wavelet. The highly accurate solutions can be readily obtained using our proposed technique. Further comparisons of our results with the previously published ones by Iwatsu et al.[9], Waheed[67], Khanafer et al.[13], and Abdelkhalek[14] for the minimum and maximum velocity components U_x and V_y at $x = 0.5$ and $y = 0.5$ in the cases of $Gr = 100$ and $Re = 100, 400$ are presented in Tables 5 and 6. An excellent agreement is found for various resolution level j from 3 to 6.

5 Effects of alternative temperature distributions

In the above analysis, our proposed approach has been verified via a series of comparisons. Here, we apply it to several different cases overlooked in the previous studies.

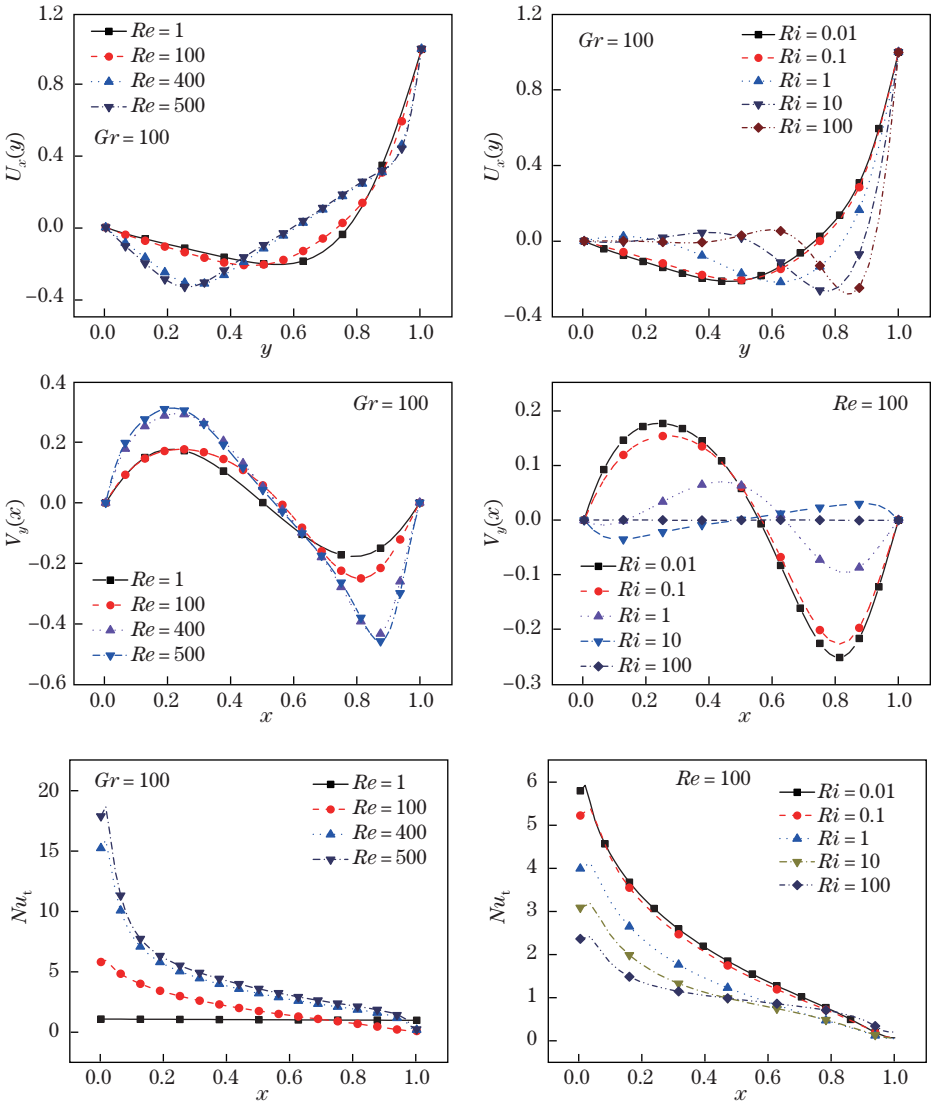

Fig. 4 Local Nusselt numbers of top lid-driven wall and velocities at vertical mid-plane $x = 0.5$ and horizontal mid-plane $y = 0.5$ with $\lambda = \gamma = 0$ (line: results by wHAM $j = 5$, points: numerical results by FVM) (color online)

Table 5 Maximum and minimum velocities U, V at midsections $x = 0.5$ and $y = 0.5$ respectively when $Re = Gr = 100$ compared with results by Iwatsu et al.[9], Waheed[67], Khanafer et al.[13], and Abdelkhalek[14]

Result	$U_{\min}$	$U_{\max}$	$V_{\min}$	$V_{\max}$
Iwatsu et al.[9]	−0.203 700 000	1.000 000 000	−0.244 800 000	0.169 900 000
Waheed[67]	−0.211 980 000	1.000 000 000	−0.251 027 000	0.177 125 000
Khanafer et al.[13]	−0.212 200 000	1.000 000 000	−0.250 600 000	0.176 500 000
Abdelkhalek[14]	−0.214 700 000	1.000 000 000	−0.248 500 000	0.170 300 000
This work ($j = 3$)	−0.374 153 816	0.987 907 540	−0.593 195 705	0.331 006 775
This work ($j = 4$)	−0.208 786 662	1.006 324 861	−0.306 304 187	0.186 844 637
This work ($j = 5$)	−0.210 092 061	1.002 456 198	−0.245 632 822	0.173 025 875
This work ($j = 6$)	−0.212 866 445	1.000 407 663	−0.251 011 094	0.176 962 659

Table 6 Maximum and minimum velocities U, V at midsections $x = 0.5$ and $y = 0.5$ respectively when $Re = 400$ and $Gr = 100$ compared with results by Iwatsu et al.[9], Waheed[67], Khanafer et al.[13], and Abdelkhalek[14]

Result	$U_{\min}$	$U_{\max}$	$V_{\min}$	$V_{\max}$
Iwatsu et al.[9]	−0.319 700 000	1.000 000 000	−0.445 900 000	0.295 500 000
Waheed[67]	−3.187 100 000	1.000 030 000	−0.441 064 000	−0.294 505 000
Khanafer et al.[13]	−0.309 900 000	1.000 000 000	−0.436 300 000	0.286 600 000
Abdelkhalek[14]	−0.310 400 000	1.000 000 000	−0.443 500 000	0.290 300 000
This work ($j = 5$)	−0.310 264 822	1.006 956 325	−0.449 819 839	0.292 839 911
This work ($j = 6$)	−0.320 187 326	1.002 311 854	−0.440 254 494	0.295 187 896

The mixed convection cavity flow considered here is subject to the stationary and thermally isolated boundary conditions on the left and right walls, and the movable and variously thermal boundary conditions on the top and bottom walls. This is to say, the temperature distribution on the bottom boundary is settled as $T_{\rm b} = T_0 + A_1$, while on the top boundary, it is given by various forms of temperature distribution including constant, linear, exponential, and sinusoidal cases,

$$T_{\rm t} = T_0 + A_2, \tag{50}$$

$$T_{\rm t} = T_0 + A_1 + (A_2 - A_1)\Big(\frac{X}{H}\Big), \tag{51}$$

$$T_{\rm t} = T_0 + A_1\frac{{\rm e} - {\rm e}^{\frac{X}{H}}}{{\rm e} - 1} + A_2\frac{{\rm e}^{\frac{X}{H}} - 1}{{\rm e} - 1}, \tag{52}$$

$$T_{\rm t} = T_0 + A_2\sin\Big(\frac{2\pi X}{H} + \xi\Big), \tag{53}$$

where T_0 is a reference temperature, A_1 and A_2 are constants, and ξ is the phase deviation.

By introducing an amplitude ratio $\epsilon = A_2/A_1 \in [0, 1]$ and setting the reference temperature difference $\Delta T = A_1$, we can obtain that the dimensionless temperature distribution on the bottom is $\theta_{\rm b} = 1$, and the dimensionless temperature distribution on the top is

(i) uniform type: $\theta_{\rm t} = \epsilon$,

(ii) linear type: $\theta_{\rm t} = 1 + (\epsilon - 1)x$,

(iii) exponential type: $\theta_{\rm t} = ({\rm e} - {\rm e}^x + \epsilon({\rm e}^x - 1))/({\rm e} - 1)$,

(iv) sinusoidal type: $\theta_{\rm t} = \epsilon\sin(2\pi x + \xi)$.

Highly accurate results obtained by our proposed technique are presented in terms of the streamline and isotherm patterns, and the velocity and temperature distributions, as well as the local Nusselt number. The parameters used here are the amplitude ratio $\epsilon = 0.5$, the inclined angle $\gamma = \pi/6$, and the phase difference $\xi = \pi/4$. Since the Richardson number provides a measure of the importance of buoyancy driven natural convection relative to lid-driven forced one, $Re = 100, Ri = 1$, and $Pr = 0.71$ are selected which are commonly used in the previous studies.

Taking Figs. 5(a) and 5(b) into consideration, the velocity profiles at $x, y = 0.5$ are nearly the same for the uniform, linear, and exponential cases, while this profile is totally different for the sinusoidal one. The flow fluctuation in the top and bottom half parts of the cavity is contrary. The local Nusselt number is an important physical quantity to evaluate the active conduction and transfer rate of losing energy. It is seen from Fig. 5(c) that on the top wall, the local Nusselt number decays gradually along the x-coordinate in the uniformly heated case. For the linearly and exponentially cases, the trend of the local Nusselt number is quite similar. It first increases as x enlarges, and after reaching a peak value, it decreases as x evolves. In the left

part of the top wall, the flow gains heat from the wall ($Nu < 0$), and the local Nusselt number reduces to zero nearly at $x = 0.25$ and $x = 0.31$. Then, the conduction direction reverses that the flow releases heat ($Nu > 0$) and the local Nusselt number reaches a maximum value around $x = 0.8$. For the sinusoidally heated case, the local Nusselt number fluctuates as x evolves. In the ranges of $x = 0 \sim 0.2$ and $x = 0.75 \sim 1$, the local Nusselt number reduces to two minimum values respectively, while it reaches the maximum value at $x \approx 0.5$. As seen in Fig. 5(d), the distributions of local Nusselt numbers along x on the bottom wall for the uniformly, linearly, and exponentially heated cases are quite similar. The uniform one is slightly higher than the others. The sinusoidally heated case exhibits different trend, which performs a much higher rate of absorbing heat from the wall except a small area near the left edge.

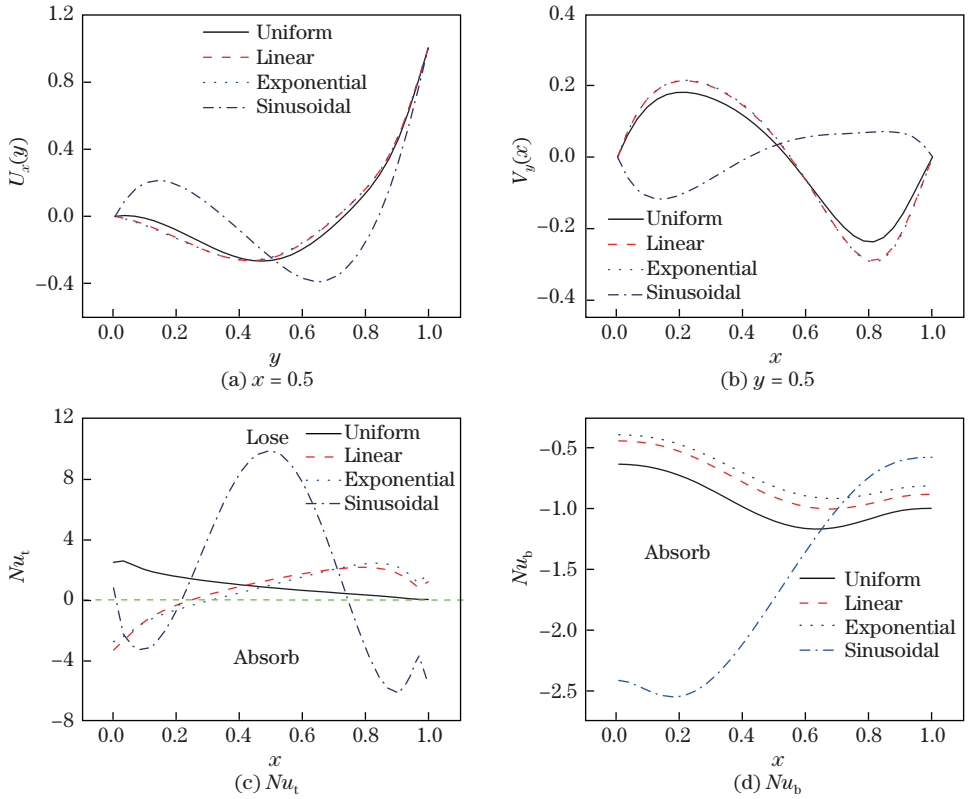

Fig. 5 Velocities at vertical mid-plane $x = 0.5$ and horizontal mid-plane $y = 0.5$, local Nusselt numbers on horizontal boundaries Nu_b, Nu_t for top sidewall uniformly, linearly, exponentially, and sinusoidally heated with $\epsilon = 0.5, \gamma = \frac{\pi}{6}$, $\xi = \frac{\pi}{4}$, and $\lambda = 0$ (color online)

To make contrast with the average Nusselt numbers, for the uniform, linear, exponential, and sinusoidal cases, their results by Eq. (45) are, respectively, 0.946, 0.683, 0.610, and 1.591 6 for the top wall, and -0.918, -0.747, -0.677, and -1.611 for the bottom wall. The actual heat absorption rate of fluid $Nu_b + Nu_t$ is 0.031 5, -0.064, -0.067, and -0.02 for those cases. From the point of view of energy conservation, when $Nu_b + Nu_t$ is negative, most of the energy generated from the bottom wall is transferred to the top wall, while only a small amount is absorbed by fluid flow consumed in dissipation of viscosity along with input energy by lid-driven wall. However, when $Nu_b + Nu_t$ is positive, it indicates that the fluid flow absorbs the kinetic energy transferred from the top moving wall. In summary, the sinusoidally heated top

lid performs the highest heat transfer rate no matter on the bottom or top boundary. That is superior to others in the same amplitude ratio, which changes the flow and temperature fields, showing superiority in heat transfer as compared with the other heating modes.

6 Effects of parameters

It is known from Eqs. (12) and (13) that there are several important non-dimensionless parameters that can affect flow and heat transfer in the cavity. Therefore, parametric studies need to be considered to cover the scale of these important parameters.

In this section, the non-dimensional temperature distribution for the sinusoidal case is given as $\theta_{\mathrm{b}} = \sin(2\pi x)$ and $\theta_{\mathrm{t}} = \epsilon \sin(2\pi x + \xi)$, which are simplified from

$$T_{\mathrm{b}} = T_0 + A_1 \sin\Big(\frac{2\pi X}{H}\Big), \quad T_{\mathrm{t}} = T_0 + A_2 \sin\Big(\frac{2\pi X}{H} + \xi\Big). \tag{54}$$

Most of our results are captured at $Pr = 0.71$ by the control variable method for different values of the amplitude ratio ϵ, the phase deviation ξ, and the inclined angle γ. The first-order iHAM technique is applied in all calculations with the convergence criterion that the relative error $E_{\mathrm{Res}} < 10^{-8}$. In Subsections 6.1 and 6.2, we figure out the effects of the amplitude ratio and the phase deviation respectively on the top wall compared with the bottom one. In Subsection 6.3, various inclined angles are investigated.

6.1 Part I: effect of amplitude ratio

In the following analysis, we simulate the uniformly heated case for $\epsilon = 0, 0.25, 0.5, 0.75, 1$, which will be used as a reference for comparison of the influence of the amplitude ratio with the sinusoidally heated case. Assume that both the top and bottom walls are heated sinusoidally for the non-uniformly heated case.

Table 7 lists the minimum ψ, the minimum velocities at $x = 0.5$, and the minimum and maximum velocities at $y = 0.5$, together with the average Nusselt numbers. It is noticed that for the uniformly heated case, as ϵ enlarges, $\psi_{\min}$ and $V_{\min}$ first decrease and then increase, while the variation of $V_{\max}$ is opposite. $U_{\min}$ and $\overline{Nu}_{\mathrm{b}}$ increase gradually, while $\overline{Nu}_{\mathrm{t}}$ decreases instantly. However, for the sinusoidally heated case, $V_{\max}$ and $\overline{Nu}_{\mathrm{t}}$ increase, but the others decrease as ϵ evolves. Besides, we notice that the heat transfer rate on the top wall (Nu_{t}) is larger than that on the bottom wall (Nu_{b}) for the sinusoidal type.

Table 7 Minimum ψ, minimum velocity at $x = 0.5$, minimum and maximum velocities at $y = 0.5$, and average Nusselt numbers in different amplitude ratios at resolution level $j = 5$ when $Gr = 10^4, Re = 100, \gamma = \frac{\pi}{6}, \xi = \frac{\pi}{4}$ with uniformly and sinusoidally heated cases 1 and 2

Case	ϵ	$\psi_{\min}$	$U_{\min}$	$V_{\min}$	$V_{\max}$	$\overline{Nu}_{\mathrm{t}}$	$\overline{Nu}_{\mathrm{b}}$	$\overline{Nu}_{\mathrm{t}} + \overline{Nu}_{\mathrm{b}}$
1	0.00	−0.081 28	−0.354 15	−0.077 97	0.042 12	1.470 96	−1.439 02	0.031 94
	0.25	−0.101 33	−0.296 55	−0.162 85	0.118 42	1.201 11	−1.165 61	0.035 50
	0.50	−0.107 66	−0.266 26	−0.237 91	0.181 65	0.946 37	−0.914 84	0.031 53
	0.75	−0.106 03	−0.237 78	−0.252 09	0.186 85	0.499 36	−0.481 59	0.017 77
	1.00	−0.102 45	−0.210 67	−0.247 75	0.175 15	0.000 00	0.000 00	0.000 00
2	0.00	−0.119 37	−0.231 82	−0.358 91	0.305 72	0.635 55	−0.859 15	−0.223 60
	0.25	−0.122 88	−0.238 35	−0.364 55	0.314 23	0.718 76	−0.976 99	−0.258 23
	0.50	−0.126 29	−0.247 63	−0.370 11	0.322 36	0.803 89	−1.095 22	−0.291 32
	0.75	−0.129 59	−0.257 59	−0.375 60	0.330 13	0.890 68	−1.213 59	−0.322 91
	1.00	−0.132 78	−0.267 72	−0.381 02	0.337 56	0.978 91	−1.331 94	−0.353 03

From the energy point of view, it is pointed out that the energy absorbed by flow from boundaries is separated into two parts. One is from the boundary moving lid by the shear force ($E_{\rm tk}$), and the other is by heat conduction from the bottom wall ($E_{\rm br}$). The energy is transferred into two directions. One part is to add the internal energy of the top wall ($E_{\rm tr}$), while the other is absorbed by the flow for the kinetic energy ($E_{\rm fk}$) and the internal energy ($E_{\rm fr}$) with the conservation relation $E_{\rm tk} + E_{\rm br} = E_{\rm tr} + E_{\rm kf} + E_{\rm fr}$. When $Nu_{\rm t} + Nu_{\rm b} < 0$, it indicates $E_{\rm br} > E_{\rm tr}$ contributing to $E_{\rm tk} < E_{\rm fk} + E_{\rm fr}$, showing that the energy absorbed from the bottom wall is transformed into the energy of flow. If $Nu_{\rm t} + Nu_{\rm b} > 0$, the situation is quite inverse that the part of the kinetic and internal energy of flow is used to be transferred into the top wall. By increasing ϵ, $Nu_{\rm t} + Nu_{\rm b}$ decreases, showing that the heat conduction is dominant, and the heat energy absorbed by fluid flow from boundary also enhances gradually at this time.

Figures 6(a) and 6(b) illustrate the variations of the local Nusselt number with x on the top and bottom walls, respectively. It is found from Fig. 6 that ϵ is only associated with the top wall and nearly has no effect on the heat transfer on the bottom wall. Moreover, the local Nusselt number on the top wall fluctuates along with x, where the direction of heat transfer at both ends is inwards ($Nu < 0$) contrary to that is outwards ($Nu > 0$) in the centre. In summary, for the sinusoidal case, the heat transfer rate increases with ϵ evolving, while the reverse point $Nu = 0$ is fixed irrelevant to ϵ as $\epsilon > 0$. When $\epsilon = 0$, the top wall is heated uniformly resulting in totally different distribution of energy transfer rate, as shown in Fig. 6(a). In this situation, not only the location of the reverse point $Nu = 0$ shifts right, but also the variational amplitude anomalously increases, which is equaling to the scale in contrast with $\epsilon = 0.5$.

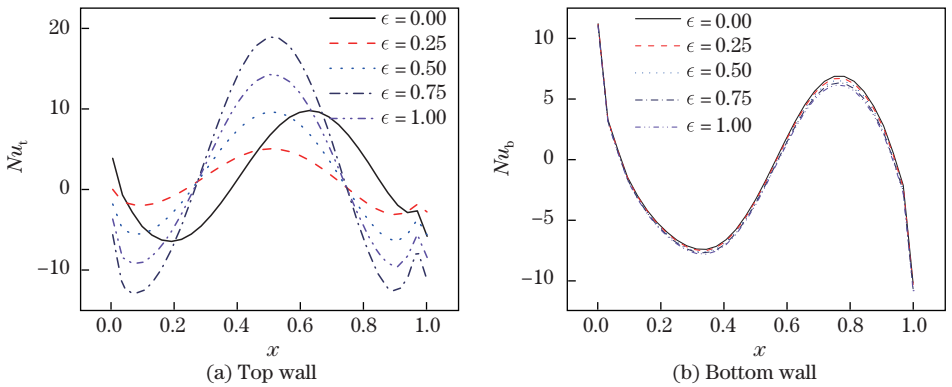

Fig. 6 Effects of amplitude ratio ϵ on local Nusselt numbers along horizontal heated and cooling walls for $Ri = 1, Re = 100, \gamma = \frac{\pi}{6}, \xi = \frac{\pi}{4}, Pr = 0.71$, and $\lambda = 0$ (color online)

6.2 Part II: effect of phase deviation

The amplitude ratio and the inclined angle are selected as $\epsilon = 1/2$ and $\gamma = \pi/6$, respectively. Figure 7 illustrates the effect of the phase deviation on velocities at midsection $x = 0.5$ and $y = 0.5$, respectively. It is seen from the figure that the change tendency along the section is almost not affected by ξ. However, the minimum velocity at $x = 0.5$ and the maximum and minimum velocities at $y = 0.5$ first increase and then decrease, reaching a maximum value around $\xi = 3\pi/4$. In conclusion, the variation in the phase deviation affects the maximum velocity value rather than its distribution to a large extent.

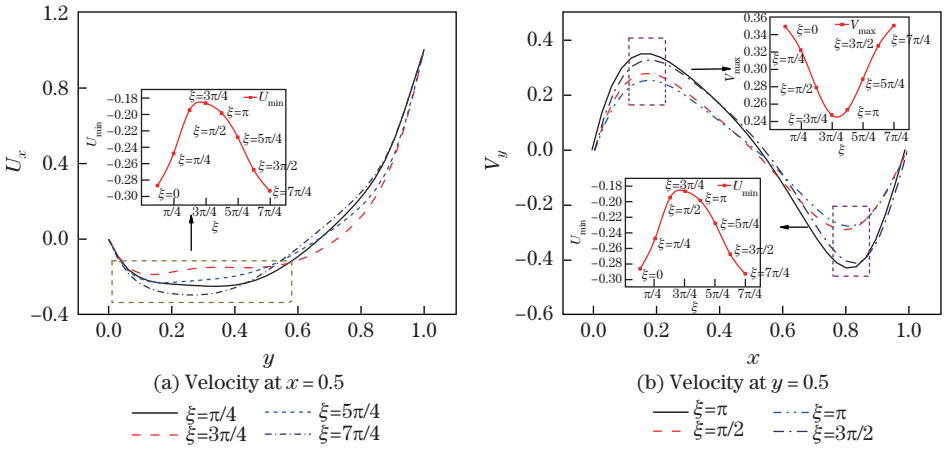

Fig. 7 Effects of phase deviation ξ on velocity at vertical mid-plane $x = 0.5$ and horizontal mid-plane $y = 0.5$ for $Ri = 1, Re = 100, \gamma = \frac{\pi}{6}, \epsilon = 0.5, Pr = 0.71$, and $\lambda = 0$ (color online)

Figures 8(a) and 8(b) demonstrate the effect of the phase deviation on the local Nusselt numbers along the top and bottom walls with the inclined angle $\pi/6$. It is seen that the local Nusselt number along the top wall is significantly influenced with the phase deviation evolving. Its profile along the top wall is approximately sinusoidal distribution and moves towards the left wall with ξ increasing, indicating that the area of heat transfer moves inwards and outwards periodically, alternately changing with each other. The maximum and minimum transfer rates are slightly affected on the bottom wall so that its variation trend is not perceived.

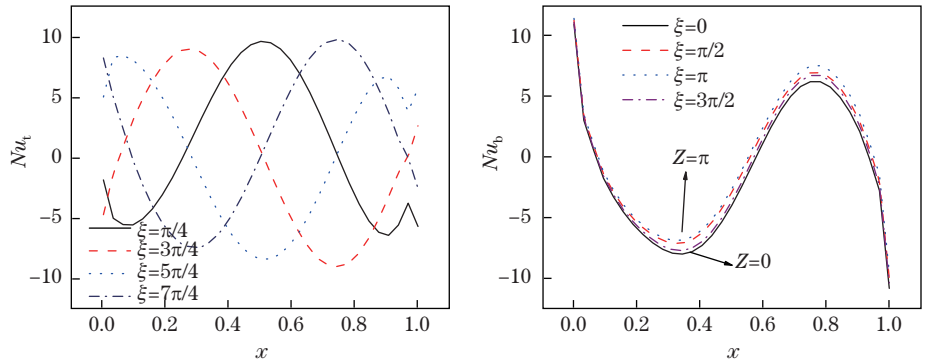

Fig. 8 Effects of phase deviation ξ on local Nusselt numbers along horizontal top and bottom walls for $Ri = 1, Re = 100, \gamma = \frac{\pi}{6}, \epsilon = 0.5, Pr = 0.71$, and $\lambda = 0$ (color online)

Figure 9 illustrates the effect of the phase deviation on the average Nusselt number for different inclined angles. As shown in Figs. 9(a) and 9(b), the fluid flow near the bottom wall acquires heat energy from the wall ($\overline{Nu}_{\rm b} < 0$) and then dissipates the energy to the top wall ($\overline{Nu}_{\rm b} > 0$) for arbitrary phases $\xi \in [0, 2\pi]$. As the phase deviation varies from 0 to 2π, which is detailed in Table 8, both the absolute values of $\overline{Nu}_{\rm b}$ and $\overline{Nu}_{\rm t}$ perform sinusoidal periodic variation, which first reduce to the minimum nearly at $7\pi/8$. Thereafter, they simultaneously and gradually increase. It indicates that heat transfer on bottom and top walls could be suppressed to the greatest extent, while the phase deviation is selected properly. Meanwhile, increasing γ is conducive to weaken the energy transfer rate on both the bottom and top boundaries, because the efficient buoyancy effect by $g\cos\gamma$ gradually decreases. As shown in

Fig. 9(c), the heat absorb rate of fluid $\overline{Nu}_{\rm b}+\overline{Nu}_{\rm t}<0$ is affected by the phase deviation and the inclined angle. When ξ evolves from 0 to 2π, its variation trend is similar to those of $\overline{Nu}_{\rm b}$ and $\overline{Nu}_{\rm t}$. However, it is irrelevant to alter the endothermic rate of fluid flow from the boundaries by increasing the inclined angles.

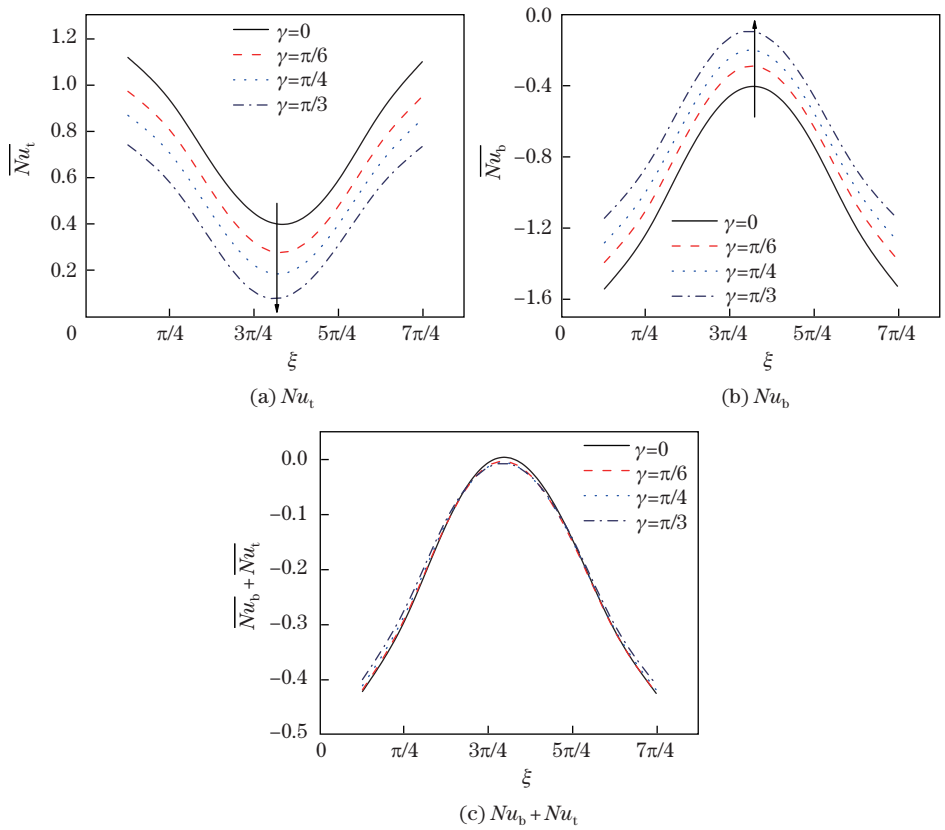

Fig. 9 Effects of phase deviation ξ on average Nusselt numbers along horizontal top and bottom walls for $Ri=1, Re=100, \gamma=0, \frac{\pi}{6}, \frac{\pi}{4}, \frac{\pi}{3}, \epsilon=0.5, Pr=0.71$, and $\lambda=0$ (color online)

Table 8 Average Nusselt numbers of top and bottom walls with different phase deviations and inclinations when $Ri=1$ and $\epsilon=0.5$

ξ	Top				Bottom			
	$\gamma=0$	$\gamma=\pi/6$	$\gamma=\pi/4$	$\gamma=\pi/3$	$\gamma=0$	$\gamma=\pi/6$	$\gamma=\pi/4$	$\gamma=\pi/3$
0	−1.117	−0.971	−0.868	−0.741	−1.540	−1.391	−1.281	−1.142 0
$\pi/4$	−0.933	−0.804	−0.705	−0.579	−1.228	−1.095	−0.989	−0.854 0
$\pi/2$	−0.661	−0.540	−0.443	−0.324	−0.779	−0.658	−0.558	−0.434 0
$3\pi/4$	−0.447	−0.322	−0.224	−0.110	−0.452	−0.333	−0.237	−0.124 0
$7\pi/8$	−0.398	−0.283	−0.192	−0.087	−0.402	−0.279	−0.185	−0.078 5
π	−0.412	−0.294	−0.208	−0.110	−0.432	−0.323	−0.238	−0.140 0
$5\pi/4$	−0.589	−0.476	−0.398	−0.310	−0.734	−0.626	−0.546	−0.453 0
$3\pi/2$	−0.879	−0.747	−0.661	−0.563	−1.189	−1.059	−0.969	−0.863 0
$7\pi/4$	−1.099	−0.949	−0.851	−0.734	−1.525	−1.375	−1.271	−1.145 0

6.3 Part III: effect of inclined angle

Here, we consider an enclosure with top and bottom walls moving simultaneously with the reverse direction $\lambda=-1$ with different inclination angles. The phase deviation and the amplitude ratio are selected as $\xi=\pi/4$ and $\epsilon=1/2$. The overall average Nusselt number on the

top and bottom boundaries, which is used to measure the overall hear transfer rate, is plotted in Fig. 10. Here, it is considered as a function of the cavity inclination angle from $0 \sim \pi/2$ with $Ri = 0.1, 1, 10$, respectively. For the forced convection regime ($Ri = 0.1$), the absolute value of the average Nusselt number decreases slowly with the inclined angle. For the mixed convection ($Ri = 1$) and the natural convection ($Ri = 10$), $\overline{Nu}_{\mathrm{b}}$ and $\overline{Nu}_{\mathrm{t}}$ decrease dramatically as the inclined angle enlarges. This is because the buoyancy effect gradually prevails in the heat transfer process. The sum $\overline{Nu}_{\mathrm{b}} + \overline{Nu}_{\mathrm{t}}$ is negative, indicating that the absolute value of average Nusselt on the top surface is smaller than that on the bottom one, which is different from the one that is identical with the uniform temperature distribution by Sharif[27]. The energy absorption rate of fluid from walls $\overline{Nu}_{\mathrm{b}} + \overline{Nu}_{\mathrm{t}}$ is irreverent to the inclined angles when $Ri \leqslant 1$, but it slightly decreases when the natural convection regime ($Ri = 10$) dominates in the heat transfer mode caused by the increase in γ.

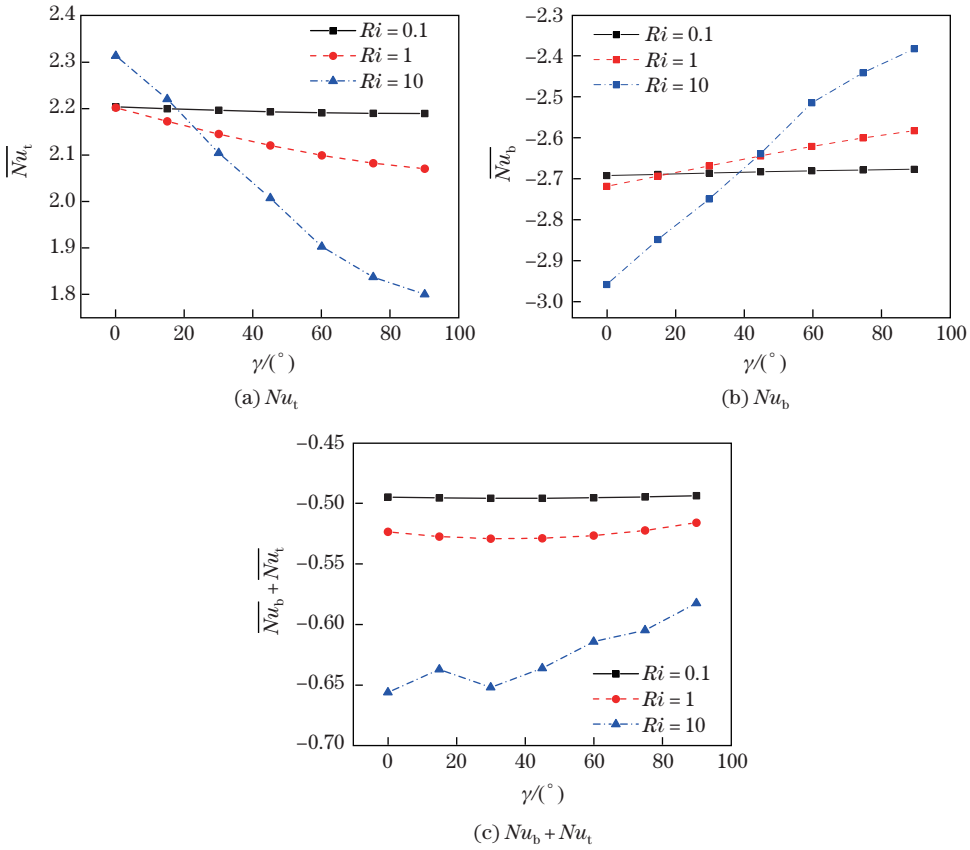

Fig. 10 Effects of inclination γ on average Nusselt of top and bottom walls and sum for $\xi = \frac{\pi}{4}, \epsilon = 0.5, Re = 100, Ri = 10$, and $\lambda = 0$ (color online)

7 Conclusions

In the present work, the wavelet-homotopy technique is developed successfully to give Coiflets wavelet solutions for the classic cavity flow and heat transfer problem with nonhomogeneous boundary conditions. It is the first time for application of the proposed technique to the problems of fluid mechanics and heat transfer. Comprehensive validations are elaborated with other numerical methods. Excellent agreement is found. Parametric physical analysis including the amplitude ratio, the inclinations, and different phase deviations is given. In addition, the

following physical findings are observed.

(i) In comparison with uniformly, linearly, and exponentially heated boundaries, sinusoidally heated horizontal walls perform the best properties of heat transfer rate under the same condition of amplitude ratio, which greatly alters the flow and temperature fields.

(ii) As the amplitude ratio increases from 0 to 1, the heat transfer rate of top wall increases, while on the bottom, it keeps the same and the reverse point $Nu = 0$ is also fixed.

(iii) Adding inclination efficiently reduces the buoyancy effect so as to weaken heat transfer rate on both walls, but it is irrelevant to alter the rate of gaining energy by the fluid from the boundaries.

(iv) Periodic variation of amplitude ratio resulting from different phase deviations contributes to approximate periodic change of heat transfer properties, while an extreme phase nearly $7\pi/8$ exists where heat transfer is suppressed to the greatest extent.

Acknowledgements Thanks to the anonymous reviewer for their constructive comments and suggestions. The authors also wish to express their thanks to the very competent reviewers for the valuable comments and suggestions.

References

[1] IDERIAH, F. J. K. Prediction of turbulent flow driven by buoyancy and shear. *ARCHIVE Journal of Mechanical Engineering Science* 1959−1982 (vols 1–23), **22**(6), 287–295 (1980)

[2] TALUKDAR, P. Mixed convection and non-gray radiation in a horizontal rectangular duct. *Numerical Heat Transfer Part A Applications*, **59**(3), 185–208 (2011)

[3] PREMACHANDRAN, B. and BALAJI, C. Conjugate mixed convection with surface radiation from a horizontal channel with protruding heat sources. *International Journal of Heat and Mass Transfer*, **49**(19/20), 3568–3582 (2006)

[4] CHAMKHA, A. J., HUSSAIN, S. H., and ABD-AMER, Q. R. Mixed convection heat transfer of air inside a square vented cavity with a heated horizontal square cylinder. *Numerical Heat Transfer Part A Applications*, **59**(1), 58–79 (2011)

[5] IMBERGER, J. and HAMBLIN, P. F. Dynamics of lakes, reservoirs, and cooling ponds. *Annual Review of Fluid Mechanics*, **14**, 153–187 (1982)

[6] OOSTHUIZEN, D. P. H. Unsteady natural convection in a partially heated rectangular cavity. *Journal of Heat Transfer*, **109**(3), 798–801 (1987)

[7] CHA, C. K. and JALURIA, Y. Recirculating mixed convection flow for energy extraction. *International Journal of Heat and Mass Transfer*, **27**(10), 1801–1812 (1984)

[8] BHUVANESWARI, M., SIVASANKARAN, S., and KIM, Y. J. Numerical study on double diffusive mixed convection with a soret effect in a two-sided lid-driven cavity. *Numerical Heat Transfer Part A Applications*, **59**(7), 543–560 (2011)

[9] IWATSU, R., HYUN, J. M., and KUWAHARA, K. Mixed convection in a driven cavity with a stable vertical temperature gradient. *International Journal of Heat and Mass Transfer*, **36**(6), 1601–1608 (1993)

[10] TORRANCE, K. E., DAVIS, R., EIKE, K., GILL, P., GUTMAN D., HSUI, A., LYONS, S., and ZEIN, H. Cavity flows driven by buoyancy and shear. *Journal of Fluid Mechanics*, **51**(2), 221–231 (2006)

[11] KHANAFER, K. M. and CHAMKHA, A. J. Mixed convection flow in a lid-driven enclosure filled with a fluid-saturated porous medium. *International Journal of Heat and Mass Transfer*, **42**(13), 2465–2481 (1999)

[12] AL-AMIRI, A. M., KHANAFER, K. M., and Pop, I. Numerical simulation of combined thermal and mass transport in a square lid-driven cavity. *International Journal of Thermal Sciences*, **46**(7), 662–671 (2007)

[13] KHANAFER, K. M., AL-AMIRI, A. M., and Pop, I. Numerical simulation of unsteady mixed convection in a driven cavity using an externally excited sliding lid. *European Journal of Mechanics-B/Fluids*, **26**(5), 669–687 (2007)

[14] ABDELKHALEK, M. M. Mixed convection in a square cavity by a perturbation technique. *Computational Materials Science*, **42**(2), 212–219 (2008)

[15] GANGAWANE, K. M. Computational analysis of mixed convection heat transfer characteristics in lid-driven cavity containing triangular block with constant heat flux: effect of Prandtl and Grashof numbers. *International Journal of Heat and Mass Transfer*, **105**, 34–57 (2017)

[16] TIWARI, R. K. and DAS, M. K. Heat transfer augmentation in a two-sided lid-driven differentially heated square cavity utilizing nanofluids. *International Journal of Heat and Mass Transfer*, **50**(9), 2002–2018 (2002)

[17] SHEREMET, M. A. and Pop, I. Thermo-bioconvection in a square porous cavity filled by oxytactic microorganisms. *Transport in Porous Media*, **103**(2), 191–205 (2014)

[18] TALEBI, F., MAHMOUDI, A. H., and SHAHI, M. Numerical study of mixed convection flows in a square lid-driven cavity utilizing nanofluid. *International Communications in Heat and Mass Transfer*, **37**(1), 79–90 (2010)

[19] CHAMKHA, A. J. Hydromagnetic combined convection flow in a vertical lid-driven cavity with internal heat generation or absorption. *Numerical Heat Transfer Part A*: *Applications*, **41**(5), 529–546 (2002)

[20] PEKMEN, B. and TEZER-SEZGIN, M. MHD flow and heat transfer in a lid-driven porous enclosure. *Computers and Fluids*, **89**(89), 191–199 (2014)

[21] AHMED, S., OZTOP, H., MANSOUR, M. A., and ABU-HAMDEH, N. MHD mixed thermo-bioconvection in porous cavity filled by oxytactic microorganisms. *Thermal Science*, **2016**, 319 (2016) https://doi.org/10.2298/TSCI16/005319A

[22] OZTOP, H. F. and DAGTEKIN, I. Mixed convection in two-sided lid-driven differentially heated square cavity. *International Journal of Heat and Mass Transfer*, **47**(8), 1761–1769 (2004)

[23] CHAMKHA A. J. and ABU-NADA E. Mixed convection flow in single- and double-lid driven square cavities filled with water-Al_2O_3 nanofluid: effect of viscosity models. *European Journal of Mechanics-B/Fluids*, **36**(10), 82–96 (2012)

[24] ISMAEL, M. A., POP, I., and CHAMKHA, A. J. Mixed convection in a lid-driven square cavity with partial slip. *International Journal of Thermal Sciences*, **82**, 47–61 (2014)

[25] SHEREMET, M. A. and POP, I. Mixed convection in a lid-driven square cavity filled by a nanofluid: Buongiorno's mathematical model. *Applied Mathematics and Computation*, **266**, 792–808 (2015)

[26] CHATTOPADHYAY, A., PANDIT, S. K., SARMA, S. S., and POP, I. Mixed convection in a double lid-driven sinusoidally heated porous cavity. *International Journal of Heat and Mass Transfer*, **93**, 361–378 (2016)

[27] SHARIF, M. A. R. Laminar mixed convection in shallow inclined driven cavities with hot moving lid on top and cooled from bottom. *Applied Thermal Engineering*, **27**(5), 1036–1042 (2007)

[28] CHENG, T. S. and LIU, W. H. Effects of cavity inclination on mixed convection heat transfer in lid-driven cavity flows. *Computers and Fluids*, **100**, 108–122 (2014)

[29] ESFE, M., AKBARI, M., KARIMIPOUR, A., AFRAND, M., HAHIAN, O., and WONGWISES, S. Mixed-convection flow and heat transfer in an inclined cavity equipped to a hot obstacle using nanofluids considering temperature-dependent properties. *International Journal of Heat and Mass Transfer*, **85**, 656–666 (2015)

[30] SIVASANKARAN, S., MALLESWARAN, A., LEE, J., and SUNDAR, P. Hydro-magnetic combined convection in a lid-driven cavity with sinusoidal boundary conditions on both sidewalls. *International Journal of Heat and Mass Transfer*, **54**(1/2/3), 512–525 (2011)

[31] AHMED, S. E., MANSOUR, M. A., and MAHDY, A. MHD mixed convection in an inclined lid-driven cavity with opposing thermal buoyancy force: effect of non-uniform heating on both side walls. *Nuclear Engineering and Design*, **265**(1/2/3), 938–948 (2013)

[32] BASAK, T., ROY, S., SINGH, S. K., and POP, I. Analysis of mixed convection in a lid-driven porous square cavity with linearly heated side wall(s). *International Journal of Heat and Mass Transfer*, **53**(9), 1819–1840 (2010)

[33] BASAK, T., ROY, S., SINGH, S. K., SHARMA, P. K., and POP, I. Analysis of mixed convection flows within a square cavity with uniform and non-uniform heating of bottom wall. *International Journal of Thermal Sciences*, **48**(5), 891–912 (2009)

[34] BASAK, T., ROY, S., and CHAMKHA, A. J. A Peclet number based analysis of mixed convection for lid-driven porous square cavities with various heating of bottom wall. *International Communications in Heat and Mass Transfer*, **39**(5), 657–664 (2012)

[35] DENG, Q. and CHANG, J. Natural convection in a rectangular enclosure with sinusoidal temperature distributions on both side walls. *Numerical Heat Transfer Part A*: *Applications*, **54**(5), 507–524 (2008)

[36] SIVASANKARAN, S., SIVAKUMAR, V., and PRAKASH, P. Numerical study on mixed convection in a lid-driven cavity with non-uniform heating on both sidewalls. *International Journal of Heat and Mass Transfer*, **53**(19), 4304–4315 (2010)

[37] SIVASANKARAN, S., SIVAKUMAR, V., and HUSSEIN, A. K. Numerical study on mixed convection in an inclined lid-driven cavity with discrete heating. *International Communications in Heat and Mass Transfer*, **46**, 112–125 (2013)

[38] HSU, T. H. and ANG, S. G. W. Mixed convection in a rectangular enclosure with discrete heat sources. *Numerical Heat Transfer Part A Applications*, **38**(6), 627–652 (2000)

[39] AL-AMIRI, A. and KHANAFER, K. Fluid-structure interaction analysis of mixed convection heat transfer in a lid-driven cavity with a flexible bottom wall. *International Journal of Heat and Mass Transfer*, **54**(17/18), 3826–3836 (2011)

[40] ABU-NADA, E. and CHAMKHA, A. J. Mixed convection flow of a nanofluid in a lid-driven cavity with a wavy wall. *International Communications in Heat and Mass Transfer*, **57**, 36–47 (2014)

[41] NASRIN, R. and PARVIN, S. Hydromagnetic effect on mixed convection in a lid-driven cavity with sinusoidal corrugated bottom surface. *International Communications in Heat and Mass Transfer*, **38**(6), 781–789 (2011)

[42] MOUMNI, H., WELHEZI, H., DJEBALI, R., and SEDIKI, E. Accurate finite volume investigation of nanofluid mixed convection in two-sided lid driven cavity including discrete heat sources. *Applied Mathematical Modelling*, **39**(14), 4164–4179 (2014)

[43] ABBASBANDY, S. and SHIVANIAN, E. Multiple solutions of mixed convection in a porous medium on semi-infinite interval using pseudo-spectral collocation method. *Communications in Nonlinear Science and Numerical Simulation*, **16**(7), 2745–2752 (2011)

[44] WILLIAMS, J. R. and AMARATUNGA, K. Introduction to wavelets in engineering. *International Journal for Numerical Methods in Engineering*, **37**(14), 2365–2388 (1994)

[45] LEWALLE, J. Wavelet transforms of the Navier-stokes equations and the generalized dimensions of turbulence. *Applied Scientific Research*, **51**(1/2), 109–113 (1993)

[46] GLOWINSKI, R., PERIAUX, J., RAVACHOL, M., PAN, T. W., WELLS, R. O., and ZHOU, X. *Wavelet Methods in Computational Fluid Dynamics*, Springer, New York (2010)

[47] YANG, Z. and LIAO, S. A HAM-based wavelet approach for nonlinear ordinary differential equations. *Communications in Nonlinear Science and Numerical Simulation*, **48**, 439–453 (2017)

[48] YANG, Z. and LIAO, S. A HAM-based wavelet approach for nonlinear partial differential equations: two dimensional Bratu problem as an application. *Communications in Nonlinear Science and Numerical Simulation*, **53**, 249–262 (2017)

[49] YU, Q., XU, H., and LIAO, S. Coiflets solutions for Föppl-von Kármán equations governing large deflection of a thin flat plate by a novel wavelet-homotopy approach. *Numerical Algorithms*, **1**, 1–28 (2018)

[50] LIU, X., ZHOU, Y., WANG, X., and WANG, J. A wavelet method for solving a class of nonlinear boundary value problems. *Communications in Nonlinear Science and Numerical Simulation*, **18**(8), 1939–1948 (2013)

[51] ZHOU, Y. H. and WANG, J. Z. Generalized gaussian integral method for calculations of scaling function transform of wavelets and its applications (in Chinese). *Acta Mathematica Scientia*, **19**(3), 293–300 (1999)

[52] ZHAO, Y., LIN, Z., and LIAO, S. An iterative ham approach for nonlinear boundary value problems in a semi-infinite domain. *Computer Physics Communications*, **184**(9), 2136–2144 (2013)

[53] GHIA, U., GHIA, K. N., and SHIN, C. T. High-*Re* solutions for incompressible flow using the Navier-Stokes equations and a multigrid method. *Journal of Computational Physics*, **48**(3), 387–411 (1982)

[54] BOTELLA, O. and PEYRET, R. Benchmark spectral results on the lid-driven cavity flow. *Computers and Fluids*, **27**(4), 421–433 (1998)

[55] BRUNEAU, C. H. and SAAD, M. The 2D lid-driven cavity problem revisited. *Computers and Fluids*, **35**(3), 326–348 (2006)

[56] MARCHI, C. H., SUERO, R., and ARAKI, L. K. The lid-driven square cavity flow: numerical solution with a 1024X1024 grid. *Joarnal of the Brazilian Society of Mechanical Sciences and Engineering*, **31**(3), 186–198 (2009)

[57] RUBIN, S. G. and KHOSLA, P. K. Polynomial interpolation methods for viscous flow calculations. *Journal of Computational Physics*, **24**(3), 217–244 (1977)

[58] SCHIREIBER, R. and KELLER, H. B. Driven cavity flows by efficient numerical techniques. *Journal of Computational Physics*, **49**(2), 310–333 (1983)

[59] VANKA, S. P. Block-implicit multigrid solution of Navier-Stokes equations in primitive variables. *Journal of Computational Physics*, **65**(1), 138–158 (1985)

[60] HOU, S., ZOU Q., CHEN S., DOOLEN, G., and COGLEY, A. C. Simulation of cavity flow by the lattice Boltzmann method. *Journal of Computational Physics*, **118**(2), 329–347 (1995)

[61] GOYON, O. High-Reynolds number solutions of Navier-Stokes equations using incremental unknowns. *Computer Methods in Applied Mechanics and Engineering*, **130**(3/4), 319–335 (1996)

[62] BARRAGY, E. and CAREY, G. F. Stream function-vorticity driven cavity solution using p finite elements. *Computers and Fluids*, **26**(5), 453–468 (1997)

[63] ZHANG, J. Numerical simulation of 2D square driven cavity using fourth-order compact finite difference schemes. *Computers and Mathematics with Applications*, **45**(1), 43–52 (2003)

[64] GUPTA, M. M. and KALITA, J. C. A new paradigm for solving Navier-Stokes equations: streamfunction-velocity formulation. *Journal of Computational Physics*, **207**(1), 52–68 (2005)

[65] ERTURK, E., CORKE, C. T., and Gökcöl, C. Numerical solutions of 2-D steady incompressible driven cavity flow at high Reynolds numbers. *International Journal for Numerical Methods in Fluids*, **48**(7), 747–774 (2005)

[66] GANZAROLLI, M. M. and MILANEZ, L. F. Natural convection in rectangular enclosures heated from below and symmetrically cooled from the sides. *International Journal of Heat and Mass Transfer*, **38**(6), 1063–1073 (1995)

[67] WAHEED, M. A. Mixed convective heat transfer in rectangular enclosures driven by a continuously moving horizontal plate. *International Journal of Heat and Mass Transfer*, **52**(21/22), 5055–5063 (2009)

[68] AHMED, S. E. Mixed convection in thermally anisotropic non-Darcy porous medium in double lid-driven cavity using Bejan's heatlines. *Alexandria Engineering Journal*, **55**(1), 299–309 (2016)

[69] PATANKAR, S. V. *Numerical Heat Transfer and Fluid Flow*, CRC Press, Boca Raton (1980)

Appendix A

$$\begin{cases} P(x,y) = -32(12\ 800x^7y(3y^2-3y+1) - 44\ 800x^6y(3y^2-3y+1) \\ \qquad -19\ 200x^5y(3y^4-5y^3-7y^2+9y-3) \\ \qquad +16\ 000x^4y(9y^4-15y^3+6y-2) \\ \qquad -2x^3y(67\ 200y^4-112\ 000y^3+35\ 200y^2+9\ 599y-3\ 200) \\ \qquad +3x^2(19\ 200y^5-32\ 000y^4+12\ 800y^3-y^2-24y+8) \\ \qquad +x(-9\ 600y^5+16\ 000y^4-6\ 400y^3+y^2+72y-24) \\ \qquad +4(-3y^3+3y^2-3y+1)), \\ Q(x,y) = -32(2\ 272x^7y^4-7\ 952x^6y^4+10\ 224x^5y^4-x^4(5\ 680y^4+1) \\ \qquad +2x^3(568y^4+1)-x^2(6y^2+1)+6xy^2-y^2) \end{cases} \tag{A1}$$

with the exact solutions

$$\theta(x,y)=16x^2(1-x)^2y^2,\quad \psi(x,y)=16x^2(1-x)^2y^2(y-1). \tag{A2}$$

Appendix B

$$\begin{aligned}
&\sum_{k'=1}^{2^j-1}\sum_{l'=1}^{2^j-1}\Big(\psi_M\Big(\frac{k'}{2^j},\frac{l'}{2^j}\Big)\mathcal{L}_\psi[h_{j,k'}(x)h_{j,l'}(y)]-\psi_{M-1}\Big(\frac{k'}{2^j},\frac{l'}{2^j}\Big)(\kappa_M\mathcal{L}_\psi[h_{j,k'}h_{j,l'}]+c_1\nabla^4[h_{j,k'}h_{j,l'}])\Big)\\
=&c_1\Big(\sum_{k=0}^{2^j}\sum_{l=0}^{2^j}R_M^\psi\Big(\frac{k}{2^j},\frac{l}{2^j}\Big)\varphi_{j,k}\varphi_{j,l}-\frac{Gr}{Re}\sum_{k=0}^{2^j}\sum_{l'=1}^{2^j-1}\theta_{M-1}\Big(\frac{k}{2^j},\frac{l'}{2^j}\Big)(h_{j,k}^{(1)}\varphi_{j,l'}\cos\gamma-h_{j,k}\varphi_{j,l'}^{(1)}\sin\gamma)\Big)\\
&+(1-\kappa_M)c_1\sum_{k=0}^{2^j}\nabla^4(\lambda h_{j,k}(x)\varpi_{j,D}(y)+h_{j,k}(x)\varpi_{j,U}(y))-(1-\kappa_M)c_1\\
&\cdot\frac{Gr}{Re}\sum_{k=0}^{2^j}\Big(\Big(\theta_D\Big(\frac{k}{2^j}\Big)h_{j,k}^{(1)}(x)\varphi_{j,0}(y)+\theta_U\Big(\frac{k}{2^j}\Big)h_{j,k}^{(1)}(x)\varphi_{j,2^j}(y)\Big)\cos\gamma\\
&-\Big(\theta_D\Big(\frac{k}{2^j}\Big)h_{j,k}(x)\varphi_{j,0}^{(1)}(y)+\theta_U\Big(\frac{k}{2^j}\Big)h_{j,k}(x)\varphi_{j,2^j}^{(1)}(y)\Big)\sin\gamma\Big),
\end{aligned}\tag{A3}$$

$$\begin{aligned}
&\sum_{k=0}^{2^j}\sum_{l'=1}^{2^j-1}\Big(\theta_M\Big(\frac{k}{2^j},\frac{l'}{2^j}\Big)\nabla^2(h_{j,k}\varphi_{j,l'})-\theta_{M-1}\Big(\frac{k}{2^j},\frac{l'}{2^j}\Big)(\kappa_M\nabla^2(h_{j,k}\varphi_{j,l'})+c_2\nabla^2(h_{j,k}\varphi_{j,l'}))\Big)\\
=&c_2\Big(\sum_{k=0}^{2^j}\sum_{l=0}^{2^j}R_M^\theta\Big(\frac{k}{2^j},\frac{l}{2^j}\Big)\varphi_{j,k}\varphi_{j,l}+(1-\kappa_M)\\
&\cdot\sum_{k=0}^{2^j}\Big(\theta_D\Big(\frac{k}{2^j}\Big)\nabla^2(h_{j,k}(x)\varphi_{j,0}(y))+\theta_U\Big(\frac{k}{2^j}\Big)\nabla^2(h_{j,k}(x)\varphi_{j,2^j}(y))\Big)\Big).
\end{aligned}\tag{A4}$$

Eventually, by multiplying $h_{j,n'}(x)h_{j,m'}(y)$ and $\varphi_{j,n}(x)\varphi_{j,m'}(y)$ on both sides of Eqs. (A3) and (A4) and then integrating on the domain [0,1] by applying the wavelet Galerkin method, some definitions were illustrated in Ref. [49]. We obtain the following coupled iterating algebra equations:

$$\begin{aligned}
\widetilde{\boldsymbol{A}}_\psi\cdot(\widehat{\boldsymbol{\Psi}}_M-\kappa_M\widehat{\boldsymbol{\Psi}}_{M-1})=&\,c_1\widetilde{\boldsymbol{B}}_\psi\cdot\widehat{\boldsymbol{\Psi}}_{M-1}+c_1\widetilde{\boldsymbol{C}}_\psi\cdot\widehat{\boldsymbol{\Theta}}_{M-1}^C+c_1\widetilde{\boldsymbol{D}}_\psi\cdot\widehat{\boldsymbol{R}}_{1M}^\psi\\
&+c_1(1-\kappa_M)(\widetilde{\boldsymbol{E}}_{1D}^\psi\cdot\widetilde{\boldsymbol{P}}_{1D}^\psi+\widetilde{\boldsymbol{E}}_{1U}^\psi\cdot\widetilde{\boldsymbol{P}}_{1U}^\psi+\widetilde{\boldsymbol{E}}_{1D}^\theta\cdot\widehat{\boldsymbol{P}}_{1D}^\theta+\widetilde{\boldsymbol{E}}_{1U}^\theta\cdot\widehat{\boldsymbol{P}}_{1U}^\theta),
\end{aligned}\tag{A5}$$

$$\begin{aligned}
\widetilde{\boldsymbol{A}}_\theta\cdot(\widehat{\boldsymbol{\Theta}}_M-\kappa_M\widehat{\boldsymbol{\Theta}}_{M-1})=&\,c_2\widetilde{\boldsymbol{B}}_\theta\cdot\widehat{\boldsymbol{\Theta}}_{M-1}+c_2\widetilde{\boldsymbol{C}}_\theta\cdot\widehat{\boldsymbol{R}}_{2M}^\theta\\
&+c_2(1-\kappa_M)(\widetilde{\boldsymbol{E}}_{2D}^\theta\cdot\widehat{\boldsymbol{P}}_{2D}^\theta+\widetilde{\boldsymbol{E}}_{2U}^\theta\cdot\widehat{\boldsymbol{P}}_{2U}^\theta),
\end{aligned}\tag{A6}$$

where the iterating tensors are

$$\begin{aligned}
&\widetilde{\boldsymbol{A}}_\psi^{\mathrm{T}}=\widetilde{\boldsymbol{B}}_\psi^{\mathrm{T}}=\widetilde{\boldsymbol{\Gamma}}_{k',n'}^{j,4}\otimes\widetilde{\boldsymbol{\Gamma}}_{l',m'}^{j,0}+2\widetilde{\boldsymbol{\Gamma}}_{k',n'}^{j,2}\otimes\widetilde{\boldsymbol{\Gamma}}_{l',m'}^{j,2}+\widetilde{\boldsymbol{\Gamma}}_{k',n'}^{j,0}\otimes\widetilde{\boldsymbol{\Gamma}}_{l',m'}^{j,4},\\
&\widetilde{\boldsymbol{A}}_\theta^{\mathrm{T}}=\widetilde{\boldsymbol{B}}_\theta^{\mathrm{T}}=\bar{\boldsymbol{\Gamma}}_{k,n}^{j,2,1}\otimes\boldsymbol{\Gamma}_{l',m'}^{j,0}+\bar{\boldsymbol{\Gamma}}_{k,n}^{j,0,1}\otimes\boldsymbol{\Gamma}_{l',m'}^{j,2},\\
&\widetilde{\boldsymbol{C}}_\psi^{\mathrm{T}}=\cos\gamma\,\widetilde{\boldsymbol{\Gamma}}_{k,n'}^{j,1}\otimes\bar{\boldsymbol{\Gamma}}_{l',m'}^{j,0,2}-\sin\gamma\,\widetilde{\boldsymbol{\Gamma}}_{k,n'}^{j,0}\otimes\bar{\boldsymbol{\Gamma}}_{l',m'}^{j,1,2},\\
&\widetilde{\boldsymbol{D}}_\psi^{\mathrm{T}}=\bar{\boldsymbol{\Gamma}}_{k,n'}^{j,0,2}\otimes\bar{\boldsymbol{\Gamma}}_{l,m'}^{j,0,2},\quad\widetilde{\boldsymbol{C}}_\theta^{\mathrm{T}}=\boldsymbol{\Gamma}_{k,n}^{j,0}\otimes\boldsymbol{\Gamma}_{l,m'}^{j,0},\\
&(\widetilde{\boldsymbol{E}}_{1D}^\psi)^{\mathrm{T}}=\widetilde{\boldsymbol{\Gamma}}_{k,n'}^{j,4}\otimes\widehat{\boldsymbol{\Gamma}}_{D,m'}^{j,0}+2\widetilde{\boldsymbol{\Gamma}}_{k,n'}^{j,2}\otimes\widehat{\boldsymbol{\Gamma}}_{D,m'}^{j,2}+\widetilde{\boldsymbol{\Gamma}}_{k,n'}^{j,0}\otimes\widehat{\boldsymbol{\Gamma}}_{D,m'}^{j,4},\\
&(\widetilde{\boldsymbol{E}}_{1U}^\psi)^{\mathrm{T}}=\widetilde{\boldsymbol{\Gamma}}_{k,n'}^{j,4}\otimes\widehat{\boldsymbol{\Gamma}}_{U,m'}^{j,0}+2\widetilde{\boldsymbol{\Gamma}}_{k,n'}^{j,2}\otimes\widehat{\boldsymbol{\Gamma}}_{U,m'}^{j,2}+\widetilde{\boldsymbol{\Gamma}}_{k,n'}^{j,0}\otimes\widehat{\boldsymbol{\Gamma}}_{U,m'}^{j,4},\\
&(\widetilde{\boldsymbol{E}}_{1D}^\theta)^{\mathrm{T}}=\cos\gamma\,\widetilde{\boldsymbol{\Gamma}}_{k,n'}^{j,1}\otimes\bar{\boldsymbol{\Gamma}}_{0,m'}^{j,0,2}-\sin\gamma\,\widetilde{\boldsymbol{\Gamma}}_{k,n'}^{j,0}\otimes\bar{\boldsymbol{\Gamma}}_{0,m'}^{j,1,2},\\
&(\widetilde{\boldsymbol{E}}_{1U}^\theta)^{\mathrm{T}}=\cos\gamma\,\widetilde{\boldsymbol{\Gamma}}_{k,n'}^{j,1}\otimes\bar{\boldsymbol{\Gamma}}_{2^j,m'}^{j,0,2}-\sin\gamma\,\widetilde{\boldsymbol{\Gamma}}_{k,n'}^{j,0}\otimes\bar{\boldsymbol{\Gamma}}_{2^j,m'}^{j,1,2},\\
&(\widetilde{\boldsymbol{E}}_{2D}^\theta)^{\mathrm{T}}=\bar{\boldsymbol{\Gamma}}_{k,n}^{j,2,1}\otimes\boldsymbol{\Gamma}_{0,m'}^{j,0}+\bar{\boldsymbol{\Gamma}}_{k,n}^{j,0,1}\otimes\boldsymbol{\Gamma}_{0,m'}^{j,2},\\
&(\widetilde{\boldsymbol{E}}_{2U}^\theta)^{\mathrm{T}}=\bar{\boldsymbol{\Gamma}}_{k,n}^{j,2,1}\otimes\boldsymbol{\Gamma}_{2^j,m'}^{j,0}+\bar{\boldsymbol{\Gamma}}_{k,n}^{j,0,1}\otimes\boldsymbol{\Gamma}_{2^j,m'}^{j,2},
\end{aligned}$$

the straight vectors are

$$\widehat{\boldsymbol{\Psi}}_M=\Big\{\psi_{p''}=\psi_M\Big(\frac{k'}{2^j},\frac{l'}{2^j}\Big)\Big\},\quad \widehat{\boldsymbol{\Theta}}_M=\Big\{\theta_{p'}=\theta_M\Big(\frac{k}{2^j},\frac{l'}{2^j}\Big)\Big\},$$
$$\widetilde{\boldsymbol{P}}^{\psi}_{1U}=\{f_{k,U}=1\},\quad \widetilde{\boldsymbol{P}}^{\psi}_{1D}=\{f_{k,D}=\lambda\},\quad \widehat{\boldsymbol{\Theta}}^{C}_{M}=-\frac{Gr}{Re}\widehat{\boldsymbol{\Theta}}_M,$$
$$\widetilde{\boldsymbol{P}}^{\theta}_{1D}=\Big\{f_{k,D}=-\frac{Gr}{Re}\theta_D\Big(\frac{k}{2^j}\Big)\Big\},\quad \widetilde{\boldsymbol{P}}^{\theta}_{1U}=\Big\{f_{k,U}=-\frac{Gr}{Re}\theta_U\Big(\frac{k}{2^j}\Big)\Big\},$$
$$\widetilde{\boldsymbol{P}}^{\theta}_{2D}=\Big\{f_{k,D}=\theta_D\Big(\frac{k}{2^j}\Big)\Big\},\quad \widetilde{\boldsymbol{P}}^{\theta}_{2U}=\Big\{f_{k,U}=\theta_U\Big(\frac{k}{2^j}\Big)\Big\},$$
$$\widehat{\boldsymbol{R}}^{\psi}_{1M}=\Big\{r_p=R^{\psi}_M\Big(\frac{k}{2^j},\frac{l}{2^j}\Big)\Big\},\quad \widehat{\boldsymbol{R}}^{\theta}_{2M}=\Big\{r_p=R^{\theta}_M\Big(\frac{k}{2^j},\frac{l}{2^j}\Big)\Big\},$$

and the suffixes are defined as

$$p=(2^j+1)k+l+1,\quad p'=(2^j+1)k+l',$$
$$p''=(2^j-1)(k'-1)+l',$$
$$m,n,k,l=0\sim 2^j,\quad m',n',k',l'=1\sim 2^j-1.$$

Then, we calculate the tensors constituted by the connection coefficients, which are split into three categories for computation. By approaching the Coiflets $h_{j,k}$ with each other, the formula is given by

$$\widetilde{\boldsymbol{\Gamma}}^{j,n}_{l,m}=\Big\{\gamma_{l,m}=\int_0^1\frac{\mathrm{d}^n h_{j,l}(x)}{\mathrm{d}x^n}h_{j,m}(x)\mathrm{d}x\Big\}. \tag{A7}$$

By the standard original Coiflets $\varphi_{j,k}$ with each other, the formula is given by

$$\boldsymbol{\Gamma}^{j,n}_{l,m}=\Big\{\gamma_{l,m}=\int_0^1\frac{\mathrm{d}^n \varphi_{j,l}(x)}{\mathrm{d}x^n}\varphi_{j,m}(x)\mathrm{d}x\Big\}. \tag{A8}$$

By the approaching Coiflets with the standard original Coiflets, they are written as

$$\bar{\boldsymbol{\Gamma}}^{j,n,1}_{l,m}=\Big\{\overline{\gamma}_{l,m}=\int_0^1\frac{\mathrm{d}^n h_{j,l}(x)}{\mathrm{d}x^n}\varphi_{j,m}(x)\mathrm{d}x\Big\}, \tag{A9}$$

$$\overline{\boldsymbol{\Gamma}}^{j,n,2}_{l,m}=\Big\{\overline{\gamma}_{l,m}=\int_0^1\frac{\mathrm{d}^n \varphi_{j,l}(x)}{\mathrm{d}x^n}h_{j,m}(x)\mathrm{d}x\Big\}. \tag{A10}$$

By the approaching Coiflets with the boundary Coiflets $\varpi_{j,S}(x)$, it is defined by

$$\begin{cases}\widehat{\boldsymbol{\Gamma}}^{j,n}_{D,k}=\Big\{\overline{\gamma}^{j,n}_{L,k}=\displaystyle\int_0^1\frac{\mathrm{d}^n \varpi_{j,\mathrm{b}}(x)}{\mathrm{d}x^n}h_{j,k}(x)\mathrm{d}x\Big\},\\ \widehat{\boldsymbol{\Gamma}}^{j,n}_{U,k}=\Big\{\overline{\gamma}^{j,n}_{L,k}=\displaystyle\int_0^1\frac{\mathrm{d}^n \varpi_{j,\mathrm{t}}(x)}{\mathrm{d}x^n}h_{j,k}(x)\mathrm{d}x\Big\}.\end{cases} \tag{A11}$$

The straight vectors of the nonlinear parts $\widehat{\boldsymbol{R}}^{\psi}_{1M}$ and $\widehat{\boldsymbol{R}}^{\theta}_{2M}$ are approximated by product of calculated vectors of ψ and θ, which are expressed by

$$\begin{cases}\widehat{\boldsymbol{R}}^{\psi}_{1M}=Re\displaystyle\sum_{s=0}^{M-1}(\widehat{\boldsymbol{\Psi}}^{s,j}_{1,0}\odot\widehat{\boldsymbol{\Psi}}^{M-1-s,j}_{0,3}+\widehat{\boldsymbol{\Psi}}^{s,j}_{1,0}\odot\widehat{\boldsymbol{\Psi}}^{M-1-s,j}_{2,1}\\ \qquad\qquad -\widehat{\boldsymbol{\Psi}}^{s,j}_{0,1}\odot\widehat{\boldsymbol{\Psi}}^{M-1-s,j}_{3,0}-\widehat{\boldsymbol{\Psi}}^{s,j}_{0,1}\odot\widehat{\boldsymbol{\Psi}}^{M-1-s,j}_{1,2}),\\ \widehat{\boldsymbol{R}}^{\theta}_{2M}=Pr\,Re\displaystyle\sum_{s=0}^{M-1}(\widehat{\boldsymbol{\Psi}}^{s,j}_{1,0}\odot\widehat{\boldsymbol{\Theta}}^{M-1-s,j}_{0,1}-\widehat{\boldsymbol{\Psi}}^{s,j}_{0,1}\odot\widehat{\boldsymbol{\Theta}}^{M-1-s,j}_{1,0}).\end{cases} \tag{A12}$$

It is worth mentioning that the effects of the nonhomogeneous boundaries involve two aspects. One is that it affects the wavelet approaching precision for ψ_0 and θ_0 via Eqs. (37) and (38). The other is that it adds the integration correction items in Eqs. (A5) and (A6),

$$\begin{cases}\widehat{\boldsymbol{\Psi}}^{M,j}_{u,v}=(\widetilde{\boldsymbol{\Phi}}^{j}_{u}\otimes\widetilde{\boldsymbol{\Phi}}^{j}_{v})^{\mathrm{T}}\cdot\widehat{\boldsymbol{\Psi}}^{U}_{M}+(1-\chi_{M+1})\widehat{\boldsymbol{P}}^{\psi,j}_{u,v},\\ \widehat{\boldsymbol{\Theta}}^{M,j}_{u,v}=(\widetilde{\boldsymbol{\Phi}}^{j}_{u}\otimes\widetilde{\boldsymbol{\Phi}}^{j}_{v})^{\mathrm{T}}\cdot\widehat{\boldsymbol{\Theta}}^{U}_{M}.\end{cases} \tag{A13}$$

Then, we take the sum according to Eqs. (23) and (24),

$$\begin{cases} \widehat{\boldsymbol{\Psi}}^j_{u,v} = \displaystyle\sum_{i=0}^{M} \widehat{\boldsymbol{\Psi}}^{i,j}_{u,v} = (\widetilde{\boldsymbol{H}}^j_u \otimes \widetilde{\boldsymbol{H}}^j_v)^{\mathrm{T}} \cdot \sum_{i=0}^{M} \widehat{\boldsymbol{\Psi}}^U_i + \widehat{\boldsymbol{P}}^{\psi,j}_{u,v}, \\ \widehat{\boldsymbol{\Theta}}^j_{u,v} = \displaystyle\sum_{i=0}^{M} \widehat{\boldsymbol{\Theta}}^{i,j}_{u,v} = (\widetilde{\boldsymbol{\Phi}}^j_u \otimes \widetilde{\boldsymbol{H}}^j_v)^{\mathrm{T}} \cdot \sum_{i=0}^{M} \widehat{\boldsymbol{\Theta}}^U_i, \end{cases} \tag{A14}$$

where the approximation of the nonhomogeneous boundary part is

$$\begin{cases} \widehat{\boldsymbol{P}}^{\psi,j}_{u,v} = (\widetilde{\boldsymbol{\Phi}}^j_u)^{\mathrm{T}} \cdot (\widetilde{\boldsymbol{P}}_{1D} \otimes \widetilde{\boldsymbol{\Phi}}^j_{v,D}) + (\widetilde{\boldsymbol{\Phi}}^j_u)^{\mathrm{T}} \cdot (\widetilde{\boldsymbol{P}}_{1U} \otimes \widetilde{\boldsymbol{\Phi}}^j_{v,U}), \\ \widetilde{\boldsymbol{H}}^j_u = \Big\{ h_s = h_{j,k}\Big(\frac{s}{2^j}\Big) \Big\}, \quad \widetilde{\boldsymbol{\Phi}}^j_u = \Big\{ \varphi_s = \varphi_{j,k}\Big(\frac{s}{2^j}\Big) \Big\}, \\ \widetilde{\boldsymbol{\Phi}}^j_{v,D} = \Big\{ \varpi_s = \varpi_{j,D}\Big(\frac{s}{2^j}\Big) \Big\}, \quad \widetilde{\boldsymbol{\Phi}}^j_{v,U} = \Big\{ \varpi_s = \varpi_{j,U}\Big(\frac{s}{2^j}\Big) \Big\}, \quad s = 0 \sim 2^j. \end{cases} \tag{A15}$$

It is pointed out that the approximate tensors of dimension are $(2^j+1)\times(2^j+1)$,

$$\widehat{\boldsymbol{F}}^U = \Big\{ f_p = f\Big(\frac{k}{2^j}, \frac{l}{2^j}\Big) \Big\}, \quad \boldsymbol{F} = \boldsymbol{\Psi}, \boldsymbol{\Theta}, \quad f = \psi, \theta.$$